PCCP

Exploring Electronic Properties of Carbon Nanoflake-based Charge Transport Materials for Perovskite Solar Cells: A Computational Study

Journal:	*Physical Chemistry Chemical Physics*
Manuscript ID	CP-ART-12-2024-004608.R1
Article Type:	Paper
Date Submitted by the Author:	19-Feb-2025
Complete List of Authors:	Li, Ruicheng; Institute of Science Tokyo, School of Materials and Chemical Technology Maeda, Keisuke; Institute of Science Tokyo, School of Materials and Chemical Technology Kameda, Keisuke ; Institute of Science Tokyo, Department of Chemical Science and Engineering, School of Materials and Chemical Technology Ihara, Manabu; Institute of Science Tokyo, School of Materials and Chemical Technology Manzhos, Sergei; Institute of Science Tokyo, School of Materials and Chemical Technology

Exploring Electronic Properties of Carbon Nanoflake-based Charge Transport Materials for Perovskite Solar Cells: A Computational Study

Ruicheng Li, Keisuke Maeda, Keisuke Kameda, Manabu Ihara[1], Sergei Manzhos[2]

School of Materials and Chemical Technology, Institute of Science Tokyo, Ookayama 2-12-1, Meguro-ku, Tokyo 152-8552 Japan

Abstract

Carbon-based materials, in particular carbon nanoflakes (CNF) and carbon quantum dots (CQD), have been increasingly used in charge transport layers and electrodes for perovskite solar cells (PSC). There are practically limitless possibilities of designing such materials with different sizes, shapes and functional groups, which allows modulating their properties such as band alignment and charge transport. Solid state packing further modifies these properties. However, there is still limited insight into electronic properties of this type of materials as a function of their chemical composition, structure, and packing. Here, we compute the dependence of band alignment and charge transport characteristics on size, chemical composition, and structure of commonly accessible types of nanoflakes and functional groups and further consider the effect of their packing. We use a combination of density functional theory (DFT) and density functional-based tight binding (DFTB) to get electronic structure level insight at length scales (nanoflake sizes) relevant to the experiment. We find that CNFs must have sizes as small as 1.3 nm to provide band alignments suitable for their use as hole transport materials with methylammonium lead iodide commonly used in PSCs. We show that both shape and functionalization can significantly modify band alignment of the CNF, by more than half an eV. Inter-flake interactions further modify the band alignment, in some cases by about half an eV. CNFs of such small sizes possess sufficient inter-flake

[1] E-mail: mihara@chemeng.titech.ac.jp . Tel.: +81-(0)3-5734-3918
[2] E-mail: Manzhos.s.aa@m.titech.ac.jp . Tel.: +81-(0)3-5734-3918

electronic coupling for efficient hole transport. In contrast, no shape or size of CNF produces band alignment suitable for use as electron transport materials.

Keywords: carbon nanoflake, carbon quantum dot, perovskite solar cell, density functional theory, density functional tight binding, charge transport material.

1 Introduction

Hybrid organic-inorganic perovskite solar cells (PSC) have been attracting great research interest in the past decade due to their relatively high power conversion efficiencies (PCE), flexibility, relative ease of synthesis of the perovskite material and ease of device fabrication. With hole transport materials (HTM) and electron transport materials (ETM), PSCs have achieved PCEs of over 25% in academic research, but remain far from commercialization due in particular to poor device stability.[1–5] For instance, hybrid organic-inorganic perovskites, such as the widely used methylammonium lead iodide ($MAPbI_3$), are highly sensitive to water, which leads to its rapid degradation under ambient environments, resulting in a significant reduction in device efficiency.[6,7] Moreover, widely used HTMs can accelerate the degradation process. HTMs such as Spiro-OMeTAD and PTAA are commonly employed to enhance device efficiency despite their high cost.[8,9] To ensure efficient hole transport, p-dopants such as Li-TFSI and tBP are often applied to improve the hole mobility of these HTMs. These molecular dopants are hydrophilic and can absorb moisture from air.[10–15] The moisture accumulated in the HTM layer can lead to perovskite degradation, counteracting the purpose of encapsulation and protection.[10,12,16–18] Though attempts have been made to develop more stable dopants, such as Cu(II) pyridine, F4-TCNQ, CO(III) and CuSCN, their high costs and complex synthetic routes are still outstanding issues.[11,16,19–24] Therefore, the development of dopant-free, non-expensive HTMs has become an important direction in resolving the bottleneck on the way to practical and large-scale application of PSCs.[25–30]

Non-fullerene-based carbon derivatives, particularly carbon nanotube (CNT) -based and carbon nanoflake (CNF) -based materials, have gained increasing attention in recent years, especially as materials for charge transport layers in PSCs.[31–47] The hydrophobicity of certain carbon materials can protect the perovskite layer from moisture degradation and greatly improve the lifetime of the device.[32,37,46,48] Furthermore, carbon-based materials can have high conductivity, allowing them to be used without dopants.[49–52] In contrast to molecular HTMs with complex and costly synthesis routes, high abundance of carbon sources makes them potentially amenable to large-scale production with relatively low cost.[46,53–55] Furthermore, carbon-based materials can be synthesized from biomass or wastes, making them also promising from the perspective of environmental remediation.[47,56–64] The significant potential of carbon-based HTMs has attracted growing research interest, prompting efforts to replace traditional HTM/gold electrodes with carbon-based materials in the development of carbon-based PSCs (C-PSC). In comparison to traditional PSCs, C-PSCs can demonstrate improved long-term stability even without encapsulation.[31,32,37,38,46,48,54] In addition, functional groups in carbon-based materials have also been reported to contribute to the crystal growth of perovskite and stability enhancement of the device.[36,65–67] Chen et al. applied oxygen-containing functional groups-decorated CNT in C-PSCs.[36] The functional groups formed strong hydrogen bonding with MA^+ in $MAPbI_3$ perovskite and obstructed the reaction between water molecules and the perovskite layer. On the other hand, the effect of functional groups on key electronic properties of charge transport, such as band alignment, reorganization energy, and electronic coupling, have not been fully elucidated. The interpretation is particularly important considering interest in synthesizing carbon-based materials from biomass and waste[47,56–64] in which case multiple functional groups may be present in an uncontrollable way.

Despite notable achievements in enhanced stability, the highest PCE of C-PSCs (over 17%) is still lower than that of the conventional PSCs (over 25%).[1,3–5,68] The carbon materials currently employed, such as CNT-based and CNF-based materials including multi-walled CNTs, carbon black and graphite, often serve as substitutes for metal electrodes and HTMs.[37–45,47,48,56–61,69,70] While modifications to their work function or conductivity have

been explored to improve charge extraction and transport, these materials still lack the hole-selectivity of traditional HTMs,[33,39–45,54,69] leading to charge recombination at the carbon/perovskite interface and limiting overall device performance. Effective and unidirectional charge transport requires proper band alignment. For HTM in PSCs, this means that HOMO of the material should approximately match the VBM (valence band maximum) of the perovskite and LUMO of the material should be (preferably much) higher than the CBM (conduction band minimum) of the perovskite.[71–74] In addition, other electronic properties including reorganization energies and electronic coupling integrals are also expected to affect the performance of charge transport materials.[75–77] However, most empirical studies use homemade or commercialized carbon materials without considering whether they are suitable for the intended application from the perspective of electronic properties.[56,61,78,70] The lack of rational selection of carbon materials to be used may contribute to the low performance of C-PSCs.

As mentioned above, the non-fullerene-based carbon materials can be roughly classified as CNT-based and CNF-based. For CNT-based materials, research on the relationship between their band structure and structural properties is relatively well established.[79–82] From the known relationship between CNT structure and its electronic structure, it is rather clear that obtaining CNT with band structure suitable for selective charge transportation in PSCs remains to be a challenging task.[79] In contrast, CNFs in principle allow a wide degree of control over band alignment by the choices of CNF sizes, shapes and functionalization. In recent years, CNF-based materials such as carbon quantum dots (CQD) and related materials such as carbon black have attracted great attention due to their easy synthesis, easy functionalization, chemical inertness and environment-friendliness. They have been applied in PSCs as electrodes or additives to the HTM/perovskite/ETM layers to enhance charge mobility.[31,46,83,84] However, as Zhou et al. pointed out in their review,[84] there is relatively limited insight into the use of CQDs as charge transport materials. When replacing existing HTMs/ETMs, carbon-based materials often lead to poor device performance due to the lack of charge selectivity.[54] For example, the size of CNFs (CQDs) currently used as HTMs for PSCs typically range in size from tens of nanometers to several micrometers,[60,70,78] far

exceeding the optimal size proposed in this study below. Devices based on these materials exhibit PCE on the order of 10%, which is significantly lower than what can be achieved by conventional HTMs i.e. Spiro-OMeTAD (in the order of 20%).[3,4,16,19] This issue can be addressed through the rational design of the materials to be used.

To understand the potential of rational design of CNF-based materials with suitable band structures and charge transfer characteristics, an electronic structure level of analysis is necessary. However, there are still few previous studies of the electronic properties of CNF-based materials, while most of them are in applications other than PSCs. Barnard et al. have explored the effect of the shape, size, edge structure, and termination of single-layer CNFs on their electronic properties in a series of studies, but not in the context of a specific application.[85–90] Moreover, modifications including functionalization and doping are also believed to have significant impact on the band structure of CNFs. In the field of photovoltaic devices, several studies have explored the effect of doping or functionalization on the electronic properties of carbon-based materials such as CQDs.[91–95] For example, Kumar et al. recently constructed models of CQDs decorated with oxygen-, nitrogen-, and sulfur-containing functional groups and evaluated their potential as HTMs.[91] However, most studies only remain at the molecular level (typically for particular molecular sizes and shapes), while a comprehensive study including the effect of CNF packing on the material's electronic structure and charge transfer integrals remains missing, which is a critical parameter that should be considered; this is done this work. Recently, several studies appeared focusing on reorganization energies of CNF or generally polyaromatic hydrocarbon (PAH) based charge transport materials[96–99] but they (as well as modeling works on CNFs for other applications[100,101]) did not consider their selection specifically for PSC, i.e. *simultaneously* the conditions of suitable HOMO and high enough bandgap in addition to reorganization energy; this is done in this work. One bottleneck in such calculation is that the consideration of packing calls for relatively large-scale models, which may be unfeasible with DFT-based methods.[102] The high cost of DFT also limits the computational scale when dealing with carbon materials for other applications, including LEDs[103], thermoelectrics[104], secondary-ion batteries[105] and electrocatalysts[106].

In this work, a combination of DFT and density functional-based tight binding (DFTB)[107] -based methods are applied to obtain electronic structure level of insight into the properties of CNF-based materials relevant for their potential use as charge transport materials in PSCs. Hybrid DFT was applied in smaller systems, while DFTB, with its frontier orbital energies calibrated to DFT (i.e. estimating DFT energies from DFTB results), was employed for larger models where hybrid DFT becomes impractical. We consider the trend in the CNF's band alignment as well as charge transfer properties in relation to their structural and compositional parameters as necessary conditions to be met for efficient charge transport. We quantify the effect of changes in shape, size, defects and functionalization on the electronic structure, band alignment, and reorganization energies of CNFs. In solid state, although those electronic properties of individual CNFs are often relatively weakly modified by van der Waals interaction, this modification can still have substantial effect on cell performance.[108] We first investigated the role of size and structural/compositional modifications on the frontier orbital and reorganization energy at a single CNF level; to evaluate the effects of packing on the band alignment, stack models with multiple CNF layers were investigated. We find that for selective charge transportation in perovskite solar cell, the size of the CNFs should be as small as 1.3 nm. The shape of the flakes significantly affects their band alignments, as well as the existence of defects and functional groups. π–π stacking reduces the band gap by about half an eV, while the effect of different stacking patterns is negligible. Charge transfer properties of the CNFs are evaluated with the Marcus theory, and we find that hexagonal CNFs with diameters of 1.3 nm can typically deliver reorganization energies on the order of 0.1 eV and charge transfer rates on the order of 10^{14} s^{-1}.

2 Methods

DFT calculations were conducted with the Gaussian16 software package[109] and the GaussView6 GUI.[110] The monolayer CNF models were optimized using B3LYP/6-31+G(d, p) calculations.[111] We confirmed that larger basis sets do not change the conclusions (see Figure S1 and S2 in Supporting Information for the results of convergence studies). To account for interactions between CNFs, we used Grimme's D3 dispersion correction.[112] To

have a consistent computational setup, the use of dispersion correction is also extended to the calculation of single CNFs. For those systems where the CPU cost of DFT was too high, DFTB calculations were performed with the DFTB+ program package.[113] Parameter set 3ob-3-1 is used for geometry optimization for all systems.[114] This parameter set is part of the Third-Order Parametrization for Organic and Biological Systems (3OB) that has been designed for Third Order Density Functional Tight Binding (DFTB3).[115] The structures were optimized until forces were below 0.02 eV/Å under the electronic temperature of 300 K. Dispersion correction based on the Lennard-Jones potential is included in the calculation for the van der Waals interactions in the system,[116,117] using parameters from the Universal Force Field (UFF).[118] As DFTB is parameterized based on GGA DFT calculations that underestimate the bandgap by about 30% due to delocalization error,[119,120] the results from Gaussian using the hybrid B3LYP functional were used to calibrate the DFTB results for achieving hybrid-DFT-like accuracy of frontier orbital energies and bandgap (see Supporting Information).

Charge transfer characteristics were evaluated using Marcus theory[121,122] whereby a charge hopping mechanism between molecular units is assumed, and the hopping rate k between electronic states i and j of molecular units is computed as

$$k = \frac{2\pi}{\hbar}|V_{ij}|^2 \frac{1}{\sqrt{4\pi\lambda k_B T}} \exp\left(-\frac{(\Delta G + \lambda)^2}{4\lambda k_B T}\right) \tag{2.1}$$

where $\hbar$ is the Plank constant, V_{ij} is the electronic coupling between i (initial) and j (final) state, k_B is the Boltzmann constant, T is the absolute temperature, ΔG is the difference in Gibbs free energies between the final and initial states, and λ is the reorganization energy. Here, we only consider charge transfer within the hole/electron transport layer, i.e. between like molecules; hence $\Delta G = 0$, and equation 2.1 can be simplified to:

$$k = \frac{2\pi}{\hbar}|V_{ij}|^2 \frac{1}{\sqrt{4\pi\lambda k_B T}} \exp\left(-\frac{\lambda}{4k_B T}\right)$$

(2.2)

The reorganization energies were computed as

$$\lambda = \left(E_0^+ - E_+^+\right) + \left(E_+^0 - E_0^0\right)$$

(2.3)

where E_0^+ is cation's energy at the geometry of the neutral molecule, E_+^+ is cation energy at optimized cation geometry, E_+^0 is the energy of the neutral molecule at cation's geometry, and E_0^0 is the energy of the neutral molecule at optimized neutral geometry.

The electronic coupling integrals were estimated from the splitting of the frontier orbital energies (upon dimer formation from individual CNFs) as[123]

$$V_{ij} = \frac{1}{2}(\epsilon_i - \epsilon_j)$$

(2.4)

where V_{ij} is the electronic coupling, ϵ_i and ϵ_j are the energies of the orbits of the dimer that derive from the HOMO (for hole transfer) or LUMO (for electron transfer) of the monomer (as it splits due to inter-CNF interactions). Known as the "energy splitting in dimer" method, this approximation is widely used because of its simplicity.[123] This is a simplistic approach, but it is sufficient for our purpose of investigating the trend of charge transfer properties in different CNFs and compare it to existing HTMs.

All CNFs considered here are hydrogen-passivated, as they are stable and have higher bandgaps than non-passivated or saturated structures (see SI, Figure S5). Multiple PAH shapes are in principle synthesizable and have been considered for various applications,[96,97,124,125] and there is a continuum between PAH molecules and what can be called a CNF or a CQD. In this work, we focus on low aspect ratio, zigzag terminated structures. Previous calculations indicate that when the number of carbon atoms allows forming such structures, they are the most stable.[125,126] We also show below that low aspect ratio is preferred from the perspective of obtaining a higher LUMO energy. Such structures

are also expected to easier crystallize than "branched" structures (see e.g. the well-known crystal structures of pyrene or coronene[127–130]), which is advantageous for charge transport.

3 Results

3.1 Effects of size and shape of carbon nanoflakes

To understand the effect of CNF size and shape on their band alignments, we investigate CNFs with different shapes and sizes with hybrid DFT. To investigate the effect of shapes, CNF models with similar number of carbon atoms ($n \approx 150$) and different shapes (hexagonal, ribbon A-C with increasing aspect ratio, see Figure 1) were constructed. Their HOMO and LUMO energies are summarized in Figure 2. For a given size *n* of the CNF, as the aspect ratio increases, the bandgap of the flake decreases due to the additional edge states occupying the bandgap (as shown in Figure 2 and S3 in Supporting Information). Therefore, low aspect ratio CNFs such as hexagonal-shaped ones with wider bandgaps are desired for selective charge transportation in solar cells and other technologies where charge transport layers are used.[103–106]

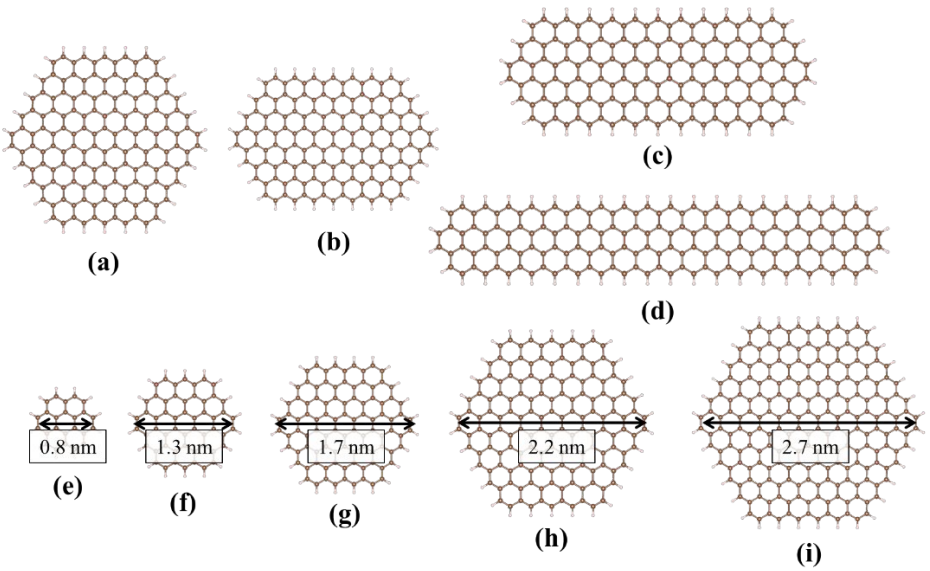

Figure 1. Models of CNFs with various shapes (hexagonal, ribbon A – C) and sizes (0.8 – 2.7 nm): (a) Hexagonal (n = 150), (b) Ribbon A (n = 144), (c) Ribbon B (n = 150), (d) Ribbon C (n = 152), (e) CNF24 (n = 24, d = 0.8 nm), (f) CNF54 (n = 54, d = 1.3 nm), (g) CNF96 (n=96, d = 1.7 nm), (h) CNF150 (n=150, d = 2.2 nm), (h) CNF216 (n=216, d = 2.7 nm).

The effect of CNF sizes was therefore studied next with hexagonal flakes with different diameters ranging from 0.8 nm to 2.7 nm. The results are also shown in Figure 2. The results indicate that CNFs with sizes smaller than 1.3 nm are required to achieve a sufficient bandgap for selective charge transportation in PSCs. As mentioned in the introduction, the sizes of CNFs (CQDs) typically used in PSCs far exceed this value,[60,70,78] although smaller sized CQDs have been reported experimentally to be synthesizable by, for example, hydrothermal methods.[131] The 1.3 nm CNF (CNF54, also known as circumcoronene[132]) also possesses a suitable HOMO level (-5.2 eV) for a match with the VBM of the perovskite (-5.4 eV). Whilst it is frequently stated that HTM's HOMO should be matched to perovskite's VBM, a more careful alignment is required. While perovskite, as is typical for inorganic semiconductors, has a negligibly small (compared to molecular HTMs) reorganization energy, the reorganization energy λ of the CNF can be substantial.[121,122] Optimal charge transport between the CNF and the perovskite is therefore expected when HOMO is offset from perovskite's valence band edge by λ. In Section 3.5 we consider the combined effect of band alignment (i.e. appropriate HOMO level and high enough LUMO level) and reorganization energy on charge transfer.

In contrast, no shape or size of CNF produced band alignment suitable for use as electron transport materials: for the LUMO to become low enough to approach the perovskite's CBM, the CNF size needs to be so large that the HOMO enters the perovskite's bandgap.

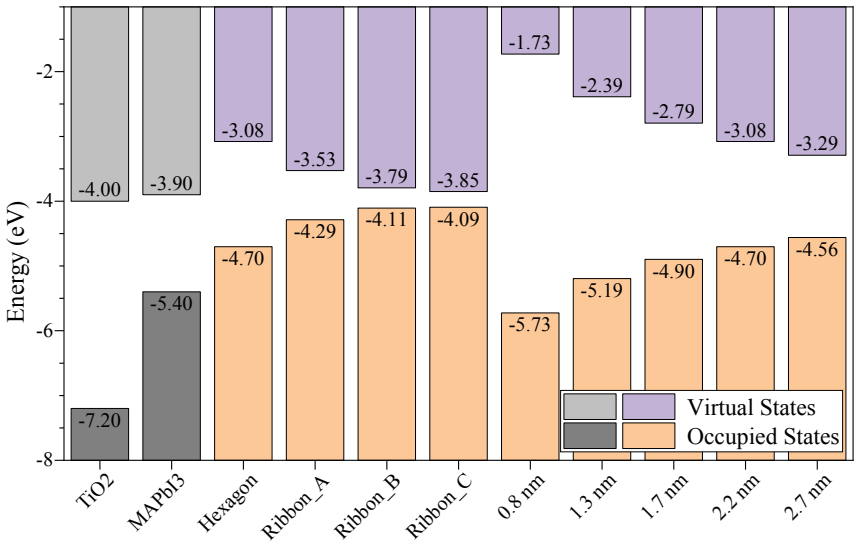

Figure 2. HOMO and LUMO of CNFs with different shapes and sizes (shown in Figure 1). The purple and orange bars represent virtual and occupied states of CNFs with different shapes (hexagonal, ribbon A – C) and sizes (0.8 – 2.7 nm), respectively; The light and dark grey bars represent virtual and occupied states of TiO_2 and $MAPbI_3$ perovskite referred from experimental research, respectively.[133]

3.2 Effects of defects

Structural defects have been widely reported in CNF-based materials. They may naturally arise during the growth of the material, or be for/med by heat, chemical, radiation, or other processes. In this section, three common zero-dimensional defects in CNFs will be discussed: single vacancies (SV), double vacancies (DV), and Stone-Wales defects (SW). We calculate their formation energies in CNFs of different sizes and analyze their impact on band alignments. Unlike in ideal models (e.g., graphene), the position of the defects in CNFs can have an impact on the above properties. In this section, we only discuss the case where the defects are located at the center of the model to avoid their interaction with the CNF edges (i.e. change in the nature of the CNF), therefore some smaller models are not considered (e.g. CNF24). We also explored the effect of defect location on formation energy and band edges in CNF96 and the results are in Supporting Information (Figure S6, S7 and S8).

For ease of presentation, we name the models with defects CNF*n-def* (as shown in Figure 3, Figure 5 and Figure 7), where *n* is the number of carbon atoms in the un-defected nanoflakes (*n* = 54, 96, 150, 216, the corresponding CNF diameters are shown in Figure 1), and *def* is the type of defects (*def* = SV, DV, SW), which are placed as close as possible to the center of the flakes. The formation energy of the defects (E_{def}^{form}) are calculated as follows:

$$E_{def}^{form} = E_{def}^{total} + n_{vac} \times \mu_{carbon} - E_{CNF}^{total} \tag{3.1}$$

Where E_{def}^{total} and E_{CNF}^{total} are the total electronic energies of CNF with and without the defect, n_{vac} is the number of carbon atom removed from the original structure to form the vacancy, and μ_{carbon} is the chemical potential of a carbon atom. We approximate μ_{carbon} as the energy of one carbon atom in graphene,

$$\mu_{carbon} = E_{carbon} + E_{coh} \tag{3.2}$$

which is estimated as the sum of the total energy of a carbon atom in vacuum (E_{carbon}, computed with DFT) and the cohesive energy of graphene (E_{coh}, taken as -7.312 eV[134]).

3.2.1 Single Vacancies

Single vacancy models are constructed by removing one carbon atom from the CNFs. The Gaussian optimized structures are shown in Figure 3.

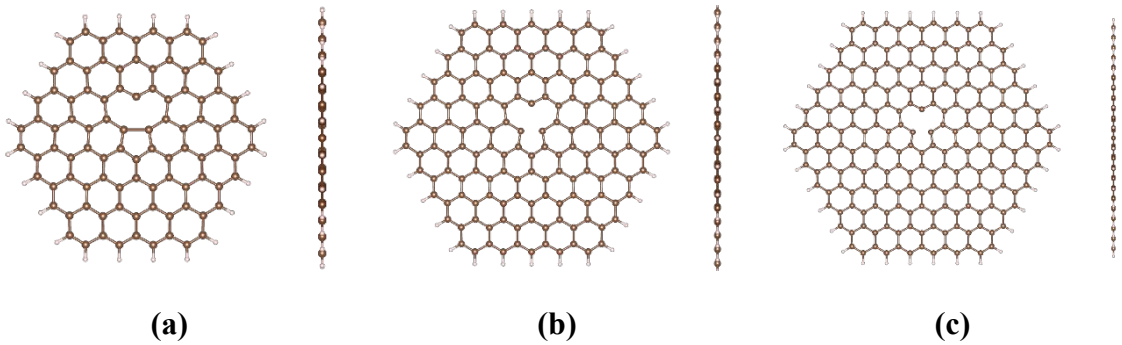

Figure 3. Front (left) and side (right) views of fully optimized CNFs with SV: (a) CNF96-SV, (b) CNF150-SV, (c) CNF216-SV.

It has been shown in previous computational and experimental studies that an SV can change the magnetic moment of graphene.[135–138] By relaxing CNF-SV models with singlet and triplet multiplicities, we find that these models have lower total energies in triplet state and the optimized structures have planar configurations. The carbon atoms around the SV rearranged due to Jahn-Teller distortion and tend to form a 5-membered ring and a 9-membered ring (V_1(5-9) defect).[135,139,140] Due to the existence of a dangling bonds of undercoordinated C atoms, SV is not thermodynamically preferred in CNFs as the defect formation energy is quite high on the order of 9 eV (as shown in Figure 4).

In Figure 4, we also report the effect of defects on the HOMO and LUMO of CNF with different sizes. In addition to slightly shifting the position of the CNF's HOMO and LUMO, the magnetic moments introduced by the dangling bonds in SVs give the system "doped-like" characteristics, which may be favored in specific applications.

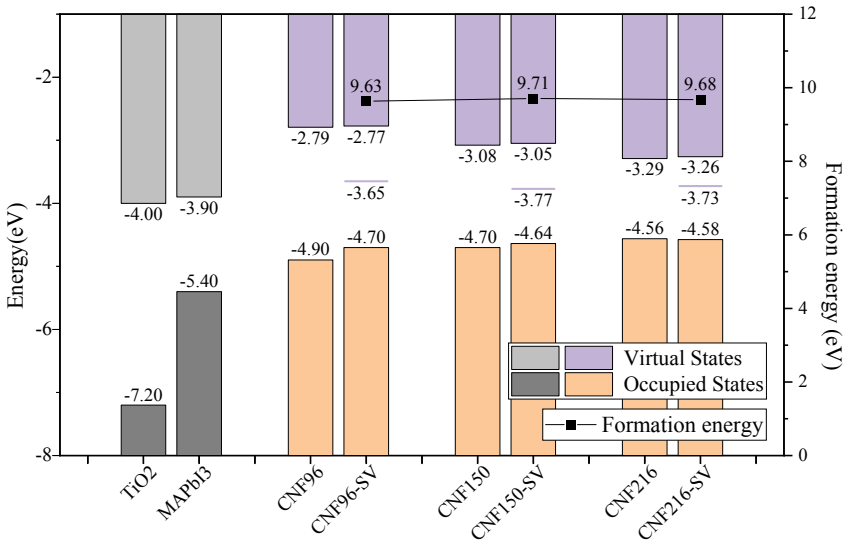

Figure 4. Left scale: HOMO and LUMO energies of CNFs with SV. The purple and orange bars represent virtual and occupied states of the CNFs, respectively. Band edges of TiO_2 and $MAPbI_3$ are shown for comparison in grey.[133] The gap states are indicated by purple lines with their energies labelled below. Right scale: corresponding defect formation energies, indicated by black squares and connecting line to help the eye.

3.2.2 Double Vacancies

Models with DV were constructed by removing two neighboring carbon atoms in CNFs with different sizes. As shown in Figure 5, in CNFs with all sizes, the carbon atoms around the removed atoms reconstructed into two 5-membered rings and one 8-membered ring, and the flakes remained planar. DV are more stable than SV due to the absence of dangling bonds in the structure. The formation energies of the two are very close (as shown in Figure 6), but since two C atoms are removed to form DV, the energy required for removing each atom is lower than that of SV, therefore DV is reported to be more common in CNF-based materials.[139] Compared to pristine CNFs, CNF-DVs have much lower LUMO energies.

Although they are still higher than the LUMO of $MAPbI_3$, the smaller band gap increases the risk of recombination and therefore is not favored for selective charge transportation.

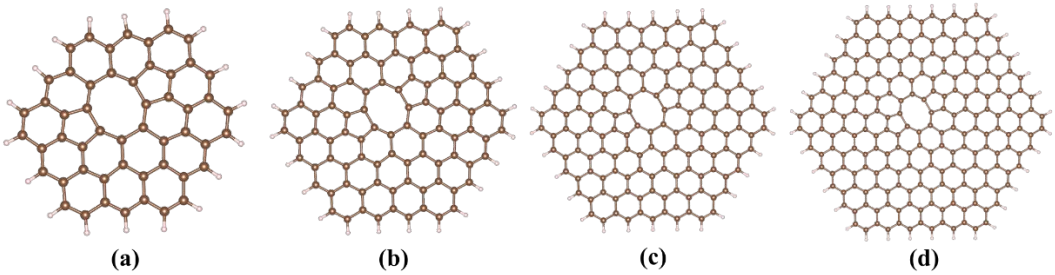

Figure 5 Fully optimized structures of CNF with DV. (a) CNF54-DV, (b) CNF96-DV, (c) CNF150-DV, (d) CNF126-DV.

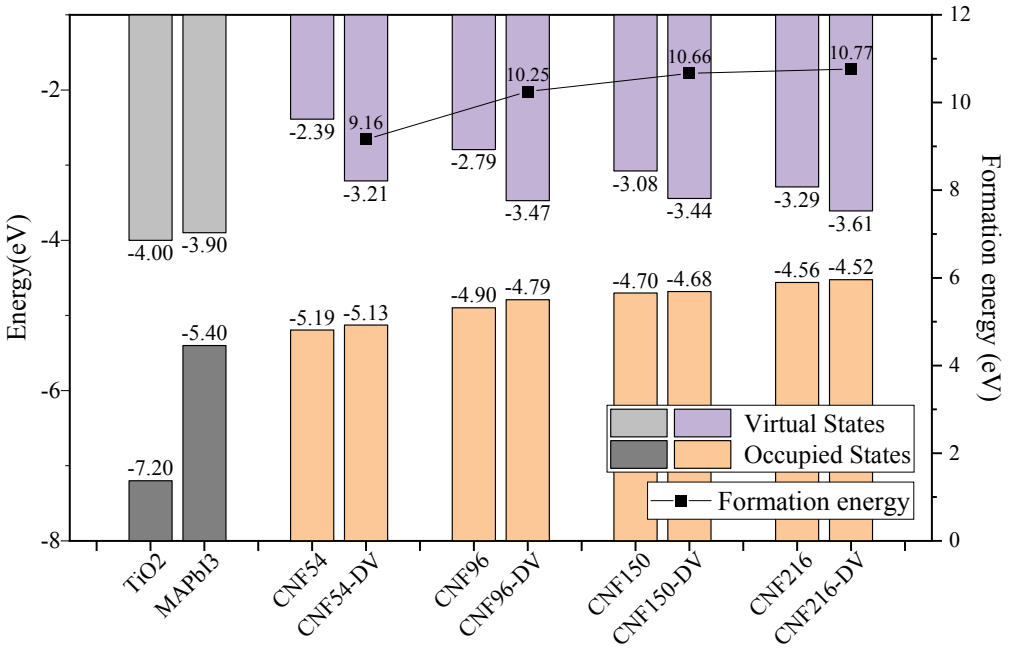

Figure 6. Left scale: HOMO and LUMO energies of CNFs with DV. The purple and orange bars represent virtual and occupied states of the CNFs, respectively. Band edges of TiO_2 and $MAPbI_3$ are shown for comparison in grey.[133] Right scale: corresponding defect formation energies, indicated by black squares and connecting line to help the eye.

3.2.3 Stone-Wales Defects

The Stone-Wales defects were introduced to the CNFs by rotating one of the C-C bonds. As shown in Figure 7, four hexagons reorientated into two 5-membered rings and two 7-membered rings, hence it is also known as 5775 or 5577 defect.[139,141–144] The defective structure maintained a planar configuration with no dangling bonds. It can be seen in Figure 8 that the formation energy for SW defect (< 5 eV) is much lower than that of SV and DV (> 9 eV), therefore it has been reported to form spontaneously during material production. In smaller systems such as CNF54, the existence of SW defects reduced the band gap by over half an eV, yet the band alignment with the perovskite remains suitable for the use as HTM. While in larger systems like CNF216, its effect on the band edges is milder and the band gap only reduced by ~0.1 eV.

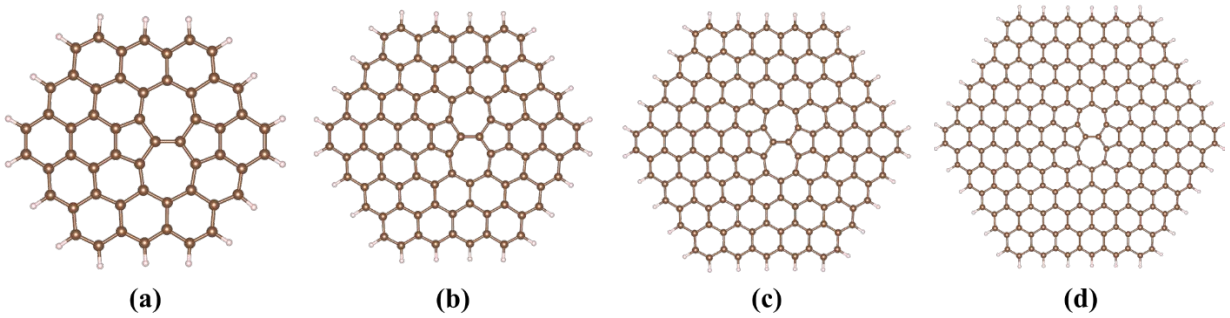

Figure 7 Fully optimized structures of CNF with SW defects. (a) CNF54- SW, (b) CNF96- SW, (c) CNF150- SW, (d) CNF216- SW.

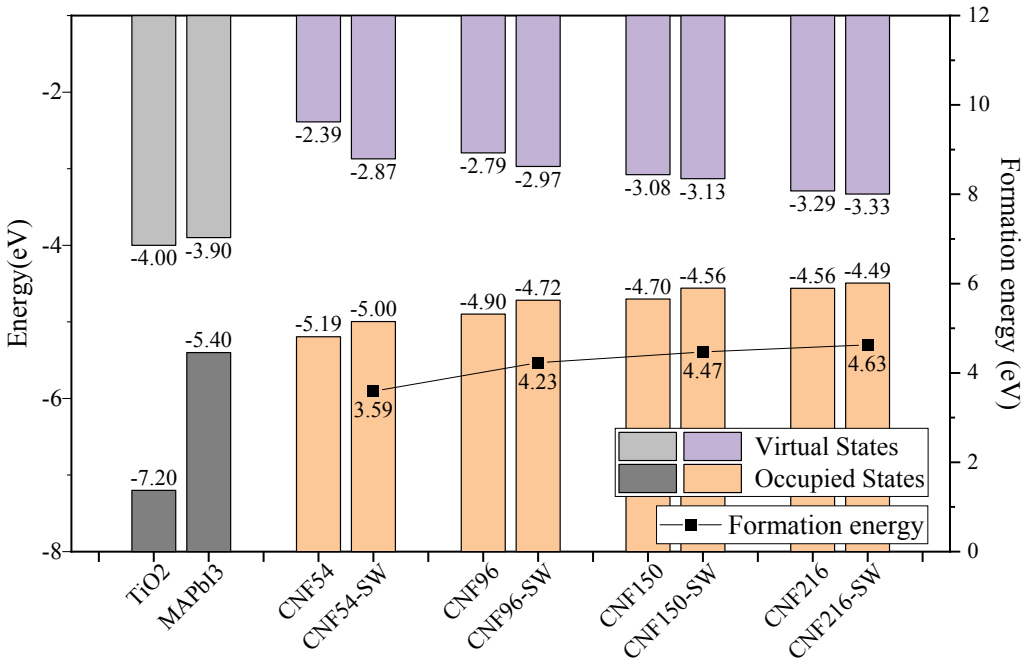

Figure 8 Left scale: HOMO and LUMO energies of CNFs with SW defect. The purple and orange bars represent virtual and occupied states of the CNFs, respectively. Band edges of TiO_2 and $MAPbI_3$ are shown for comparison in grey.[133] Right scale: corresponding defect formation energies, indicated by black squares and connecting line to help the eye.

In conclusion, all three defects studied in this section (SV, DV and SW) reduced the bandgap of the CNF and therefore are not desired for selective charge transportation. However, the formation energies of all these defects are high, and therefore they will no longer be considered in the following calculations.

3.3 Effect of functionalization

In this section, we discuss the effect of functionalization on the CNF band alignment. We modified the CNF by adding functional groups that are commonly observed in experiments or reported to have strong effects on HOMO and LUMO, as well as p-type and n-type substitutional doping.[145–149] We show here the results for the case of functionalization of CNF54 because the nanoflake of this size was shown above to have the most suitable band alignment for the use as HTM. Similar to the previous section, we named the models after

CNF54-*modi*, where -*modi* represents the type of modification (-*modi* = -CH_3 as methyl group, -OH as hydroxyl group, -COOH as carboxyl group, -CN cyano group, -NH_2 as amino group, -SO_3H as sulfo group, -O as epoxide, -N_{pyrid} as pyridinic nitrogen, -N_{pyrro} as pyrrolic nitrogen, -N_{graph} as graphitic nitrogen and -B_{graph} as boron-doped).

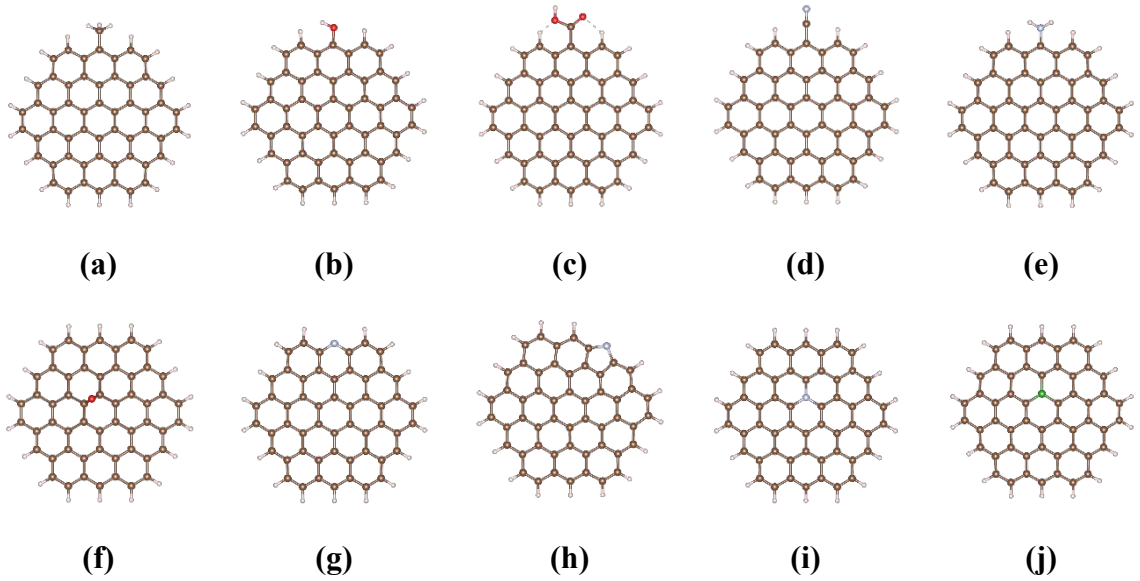

Figure 9 Fully optimized structures of functionalized CNFs. (a) CNF54-CH_3, (b) CNF54-OH, (c) CNF54-COOH, (d) CNF54-CN, (e) CNF54-NH_2, (f) CNF54-O, (g) CNF54-N_{pyrid}, (h) CNF54-N_{pyrr}, (i) CNF54-N_{graph}, (j) CNF54-B.

As shown in Figure 9, all CNF models remained planar after geometry optimization with hybrid DFT. The HOMO and LUMO energies of modified CNFs are illustrated in Figure 10. For the functionalized models, the result shows that the addition of functional groups reduced the band gap by a maximum of 0.36 eV (in the case of epoxide), which will barely affect their electron-blocking properties as the LUMO remains far above the CBM of the perovskite. Thus, their effect on the HOMO (as well as the charge transfer integral, see below) of the CNF becomes the dominant criteria for functional group selection. Most functional groups upshifted the HOMO level, and the -OH group has the most significant effect of 0.13 eV. Large energy differences with the perovskite's VBM will increase the energy loss during hole extraction, and therefore should be avoided in the case of HTMs. The charge transfer

rate at the interface with the perovskite will also suffer if the band offset exceeds the reorganization energy.[150–152] Meanwhile, certain functional groups (e.g. -CN and -COOH groups) have strong electron-withdrawing properties, therefore downshifted both the HOMO and LUMO of CNF.[153–156] Considering that the HOMO of CNF is expected to be elevated after solid state packing (see below) which may worsen its alignment with perovskite, the addition of the electron-withdrawing groups can be used to tune the band alignment between the perovskite's VBM and the CNF's HOMO without changing the size of the CNF.

In the doped systems, the pyridinic nitrogen showed similar but milder effect with the -CN group of lowering both HOMO and LUMO of the CNF. The pyrrolic and graphitic nitrogen slightly lowered the LUMO while the variation in HOMO (~0.01 eV) is insignificant compared with the pristine CNF54. As expected, they create a n-doping effect that introduces an occupied state into the original bandgap, which is considered to be disadvantageous to the electron blocking property of the material, and therefore should be avoided for applications such as selective hole transportation. Similarly, graphitic boron doping introduced an unoccupied molecular orbit into the bandgap. Boron substitution increases the hole population in the carbon material, therefore is widely used to achieve more efficient hole extraction in experiments.[40,41,157] However, it's worth mentioning that graphitic boron also upshifted the HOMO of the molecule, which can be detrimental as mentioned earlier. In the following sections, we will further discuss the effects of these modifications on charge transportation properties of CNFs.

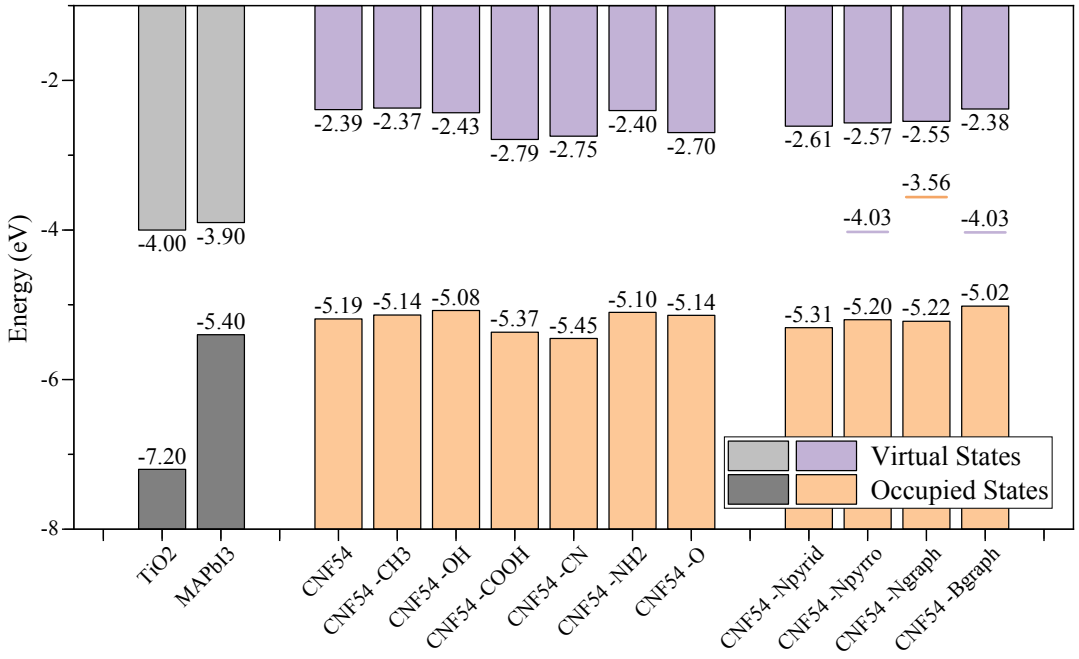

Figure 10. HOMO and LUMO of the modified CNFs. The light and dark grey bars represent virtual and occupied states of TiO_2 and $MAPbI_3$ inferred from experimental research, respectively.[133] The purple and orange bars represent virtual and occupied states of the modified CNFs, respectively. The virtual and occupied gap states in the doped systems are indicated by purple and orange lines, respectively, with their energies labelled above.

In conclusion, we found that with functionalization or doping the position of the CNF's LUMO remains suitable for use as HTM. The risk lies more in losing the alignment between CNF's HOMO and the VBM of perovskite. Specific functional groups (e.g. -CN group and -COOH group) can be used to restore such alignment as they downshift both HOMO and LUMO of the CNF. Figure S9 and S10 in SI shows that when the number of functional groups (-CN) further increases, their effect on the HOMO and LUMO of the flake also increases, while the band gap of the material decreases. When the number of -CN groups in CNF54 increase to 6, its LUMO comes below the VBM of $MAPbI_3$ perovskite and therefore in theory can be used as ETM. This extreme example demonstrates the high degree of freedom in adjusting band edges using functional groups. By adjusting the concentration of functional

groups, one can adapt the CNF more to its application, whether it is PSCs with different kinds of perovskite or other applications where hole transport layers are used.[158–164]

3.4 The effect of packing

In the previous sections, we discussed the effects of different structures and modifications on the electronic properties of single CNFs. However, in devices, CNF-based materials are typically used as solid layers. These materials may lack long-range ordering, but at short range, one typically finds ordered aggregation of CNF layers due to the interlayer van der Waals interactions and π–π stacking characteristic of polyaromatic molecules such as CNFs.[108,165] It is this stacking that is expected to have the strongest influence on the electronic properties of the material, including energy band alignment and charge transport properties. In particular, the stacked configurations are expected to determine the "ceiling" of the charge hopping rate (the highest rate in the direction of the stacking) and can therefore be used to estimate charge transport ability, even before other hopping paths, which may not be known unless the true experimental solid state structures are considered. In this section, we analyze the stacked models of CNF with hybrid DFT and DFTB calibrated to hybrid DFT (see Method) to explore the effect of different stacking patterns and number of stacked layers on their band alignment. Furthermore, we introduce modifications (functional groups) that are commonly reported in experimental research or showed interesting properties in the previous sections to further explore their effects on the structural and electronic properties of the stacked models. Finally, we estimate the inter-flake charge transfer integrals and rates.

3.4.1 Effects of stacking

The most common natural graphite stacking patterns are hexagonal (or Bernal, ABAB...) and rhombic (ABCA...).[166] To explore the effect of these patterns on the band alignment, we constructed 4-layer stacking models of the two patterns (ABAB and ABCA) with CNF54 and optimized the structures with DFTB. The frontier orbital energies from DFTB were calibrated with hybrid DFT (i.e. hybrid DFT-like energies are predicted from DFTB energies) (see Figure S12 in Supporting Information). The fully relaxed structures and their band diagrams are shown in Figure 11 and Figure 12, respectively. The DFTB optimized structures

stably maintained the stacking patterns with interlayer distances of about 3.5 Å. As shown in Figure 12, energy difference of the frontier orbitals between the two stacking patterns are negligible (~0.01 eV). The band gap of the 4-layer stack models is reduced by about half an eV compared to that of the single CNF54 flake. The upshifted HOMO in the stacked models is the main reason for such reduction. Apart from that, a minor upshift in LUMO is also observed in the stacked CNFs from Figure 12. Such phenomenon is found in both DFT and DFTB results and therefore is not considered to be due to computational errors.

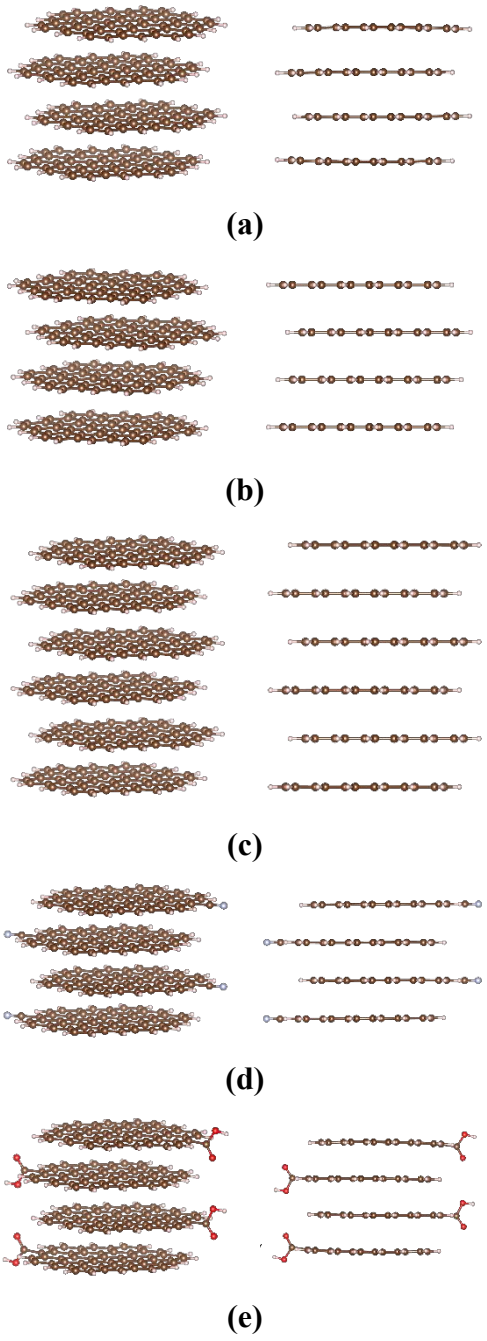

Figure 11. 3D (left) and side (right) view of DFTB optimized structures of CNF54 stacks with different stacking patterns (top row): (a) CNF54 ABAB, (b) CNF54 ABCA; AB stacked CNF54 with increased number of layers (middle row): (c) CNF54 AB 6 layers; and functionalized CNF54 ABAB (bottom row): (d) CNF54 ABAB-CN and (e) CNF54 ABAB -COOH.

In real carbon materials e.g. carbon black, the graphene-like domains may contain more than 4 parallel CNF layers.[165,167,168] We prepared AB stacked models with 6, 8, 10 and 12 layers to estimate the change in bandgaps in larger structures. The optimized 6 layer model is shown as an example in Figure 11, while the rest of the structures can be found in SI. Their frontier orbital energies are shown in Figure 12. As the number of layers increased, HOMO of the stacks continued to move upward and showed a tendency to converge, while the LUMO also slightly upshifted. The bandgap of the largest 12-layer stack (2.32 eV) remained over 80% of that of the single CNF54 flake, but its HOMO shifted upward by 0.66 eV. The loss of HOMO alignment with the perovskite's VBM due to solid state packing of molecules selected based on single-molecule properties could therefore significantly affect solar cells performance. As shown in section 3.3, certain electron withdrawing functional groups can be used to modulate the HOMO alignment. We stacked the -CN and -COOH functionalized CNF54 into 4-layered ABAB models and optimized them with DFTB. The final structures are shown in Figure 11. Noticeably, the addition of -COOH groups introduced a curvature to the flakes, which may lead to a reduction in the bandgap. Figure 12 shows that the -CN and -COOH groups downshifted the HOMO of the stacks by 0.43 eV and 0.2 eV, respectively, while the LUMO remained high enough to maintain their electron blocking properties. Therefore, from the perspective of HOMO-LUMO positions, -CN decorated CNF54 is expected to be able to function as HTM for $MAPbI_3$ perovskite solar cell in solid state.

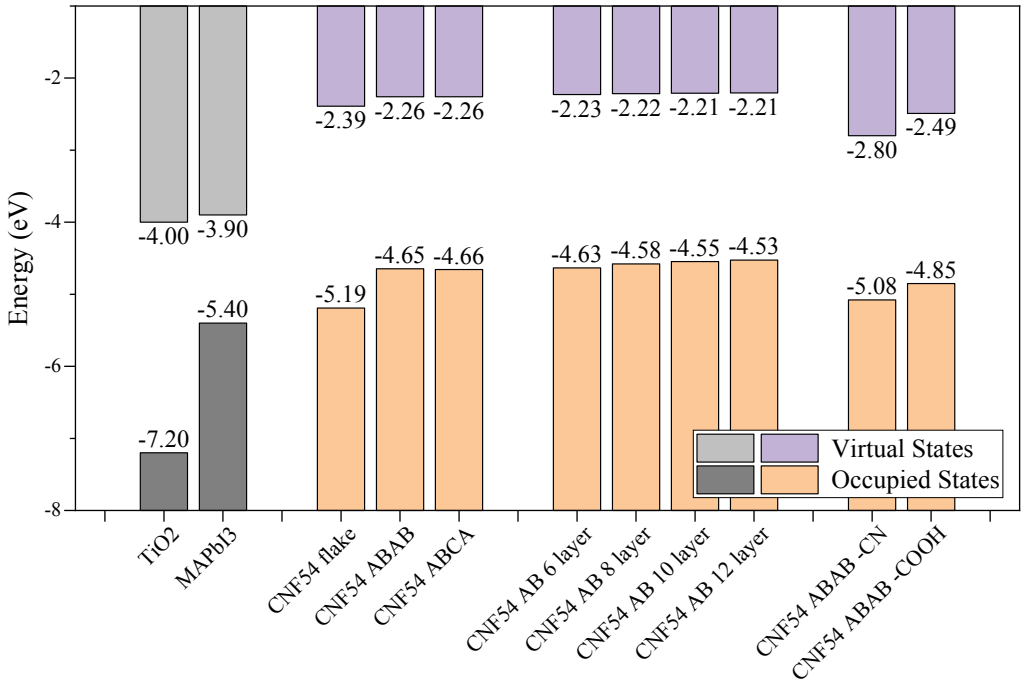

Figure 12. HOMO and LUMO energies of stacked CNF54 models with different stacking patterns, different number of stacked layers and functionalizations. The purple and orange bars represent virtual and occupied states of the CNFs, respectively. For comparison, the light and dark grey bars represent virtual and occupied states of TiO_2 and $MAPbI_3$ inferred from experimental research.[133]

3.5 Charge transport characteristics

As can be seen in the previous sections, the band structure of CNF-based materials is more suitable for use as HTM (rather than ETM) in PSCs, while HTMs are also a major obstacle on the way to the commercialization of PSCs. Therefore, in this section we only discuss the parameters related to hole transport properties, namely the reorganization energy λ_{hole} and dependent on it charge transfer rate k_{ht}. In this work, we focus on the charge transfer within the hole/electron transport layer (i.e. $\Delta G = 0$), therefore reorganization energy (λ) and electronic coupling integral (V_{ij}) become the two key parameters in calculating k. In the following sections, we will discuss the effect of different CNF structures and compositions on these parameters. We will focus on round-shaped CNFs with different sizes,

functionalizations and doping, as ribbon-shaped and defected CNFs are not preferred for selective charge transportation.

The overall hole conductance will also depend on weighted contributions of different hopping paths in solid-state materials.[169] While finding the correct packing (which may not be unique depending on fabrication conditions) is a formidable task in itself,[170,171] here we are interested in charge transfer characteristics imposed by the molecular composition and structure; we consider π–π stacking which is typically present in real CNF-based materials and which provides the direction of the highest hopping rate which largely determines and limits the overall rate. This is the rate that we consider here as a characteristic based on which optimal molecular composition and structure (CNF size) can be selected.

3.5.1 Reorganization energy

The reorganization energy is the energy required to stabilize the structure as the molecule gains/loses electrons. As can be seen from Eq. 2.2, a smaller λ_{hole} will lead to larger k_{ht}. Also, small λ means less driving force is required for exciton dissociation, which is needed for good charge transport.[172] Here, λ_{hole} was calculated for three groups of molecules: unmodified round-shaped CNFs with different sizes, CNF54 with different functional groups, and CNF54 with different dopants, as CNF54 appears to have the most suitable band alignment as shown above. Meanwhile, the λ_{hole} of Spiro-OMeTAD was also calculated at the same level of theory for comparison. The results are shown in Figure 13.

For CNFs with different sizes, it can be clearly seen that λ_{hole} tends to decrease as the size of the CNF increases. This may be related to the larger size imparting to the molecule more stiffness and therefore reducing the λ_{hole}. Compared to Spiro-OMeTAD, CNF with all sizes have significantly lower λ_{hole}, which indicate potentially better hole transport properties. For the functionalized CNF54 molecules, most functional groups slightly increased λ_{hole}. It is noteworthy that the -CN group slightly decreases λ_{hole}, while the -NH_2 group substantially increases it. This agrees with the effects of these functional groups reported for other molecules as reported in previous studies.[75,173–175] In the doped systems, the pyridinic nitrogen did not exhibit any effect on the value of λ_{hole}, graphitic and pyrrolic

nitrogen slightly reduced the λ_{hole}, while boron doping slightly and significantly reduced the λ_{hole}, respectively.

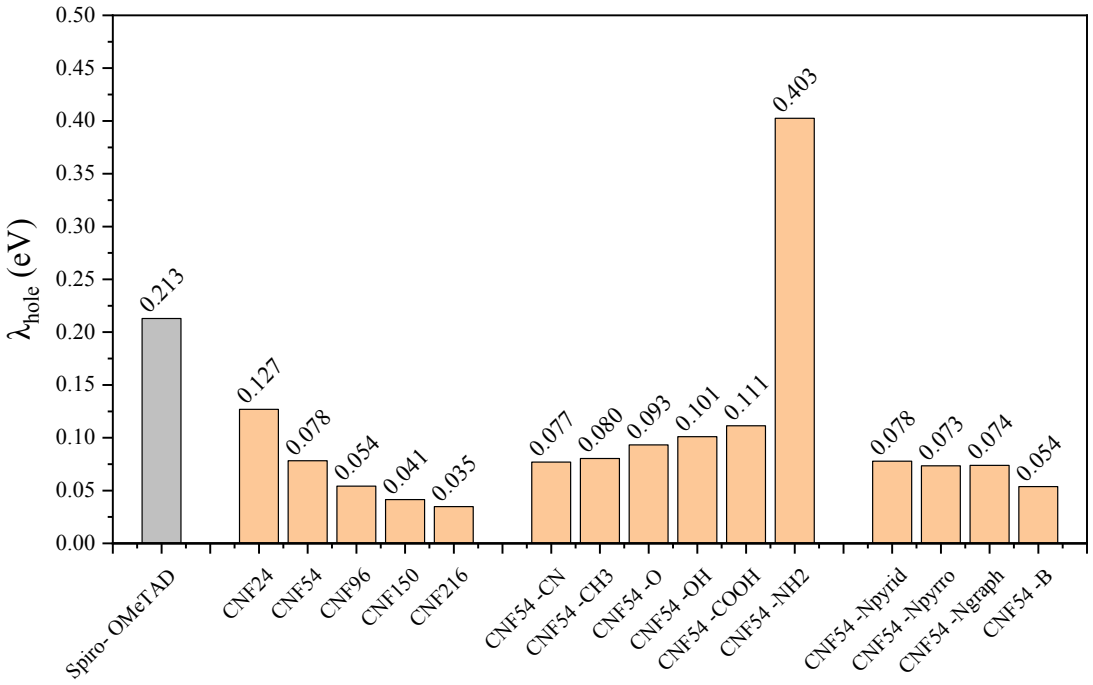

Figure 13. Reorganization energies for CNF molecules with different sizes, functional groups and dopants. The corresponding structures are given in Sections 3.1 and 3.3.

In summary, most of the CNFs possess lower reorganization energies than Spiro-OMeTAD, even with the detrimental effects from functional groups. Therefore, from the perspective of reorganization energy and the band alignment considered above, nanometer-sized and functionalized CNF-based materials with sizes on the order of 1 nm have potential to be applied as HTMs.

3.5.2 Electronic coupling integral and hole transfer rate

In this section, we evaluate the charge transport properties of the CNF-based materials from two aspects: electronic coupling integral (V_{ij}) and hole transfer rate (k_{ht}). Five molecules were selected as samples: CNF24, CNF54 and CNF96 to study the trend of charge transport properties with CNF size, along with two promising (as indicated in sections above)

functionalized CNF54 molecules (CNF54-CN and CNF54-COOH) to evaluate the effect of those functional groups. As charge transport rate calculations are sensitive to approximations,[176,177] calculations using the same approximations were also performed for Spiro-OMeTAD for comparison. The Spiro-OMeTAD dimer was optimized at the B3LYP/LanL2DZ level of theory, while the orbital energies were obtained from a single point energy calculation with B3LYP/6-31+G(d, p). The charge transfer properties are strongly affected by the packing motifs of the molecules. Due to the lack of structural information of CNF materials in solid state, here, we use π–π (AB) stacked dimers to evaluate the maximum charge transport ability for the material (while the dimer structure of Spiro-OMeTAD was taken from the work of Shi et al.[178]). Hybrid DFT is used for geometry optimization of the dimers. The final structures are shown in Figure 14. We estimate the electronic coupling integral from the energy split between two HOMO-derived dimer orbits (see equation 2.4), and the hole transfer rate from the Marcus theory, equation 2.2. The results along with the corresponding reorganization energies are summarized in Table 1.

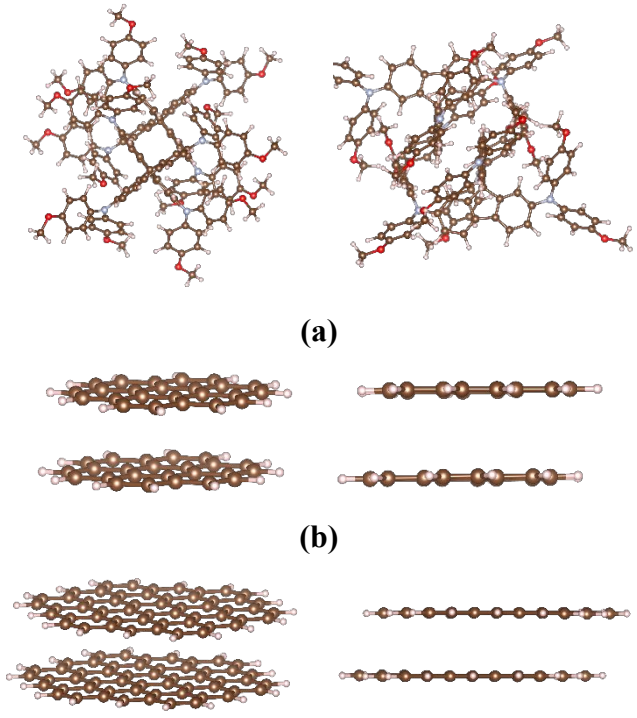

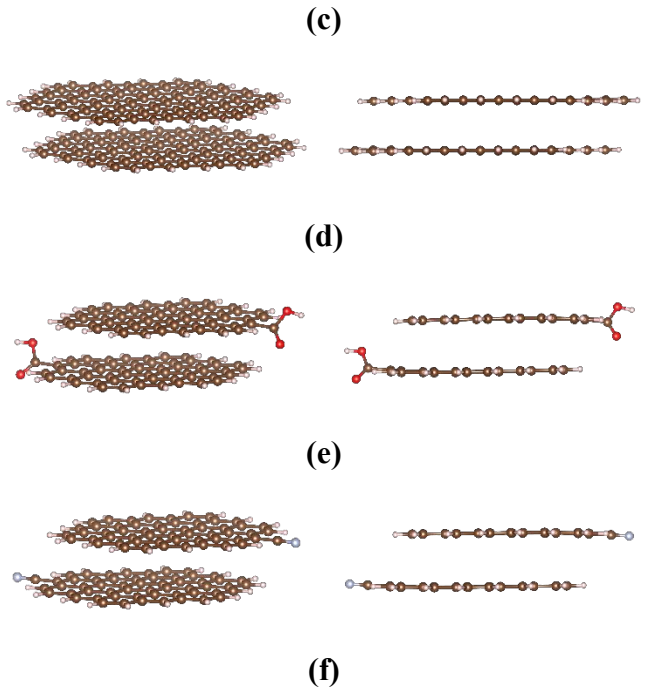

Figure 14. 3D (left) and side (right) view of hybrid DFT optimized dimer structures of: (a) Spiro-OMeTAD (initial structure was taken from reference [178]), (b) CNF24 AB, (c) CNF54 AB, (d) CNF96 AB, (e) CNF54-COOH and (f) CNF54-CN.

Table 1. Reorganization energies (λ_{hole}), electronic coupling integrals (V_{ij}) and hole transfer rates (k_{ht}) of Spiro-OMeTAD, CNF24, CNF54, CNF96, CNF54-CN and CNF54-COOH.

	$\boldsymbol{\lambda_{hole}}$ **(eV)**	$\boldsymbol{V_{ij}}$ **(eV)**	$\boldsymbol{k_{ht}}$**(s^{-1})**
Spiro-OMeTAD	0.213	0.058	1.55×10^{13}
CNF24	0.127	0.166	3.78×10^{14}
CNF54	0.078	0.137	5.25×10^{14}
CNF96	0.054	0.112	5.40×10^{14}
CNF54 -CN	0.077	0.141	5.70×10^{14}
CNF54 -COOH	0.111	0.148	3.73×10^{14}

The key result from Table 1 is that CNFs obtain an order of magnitude higher charge transfer rates than Spiro-OMeTAD. This is due to both a lower reorganization energy and a

larger transfer integral. From the results of CNF24, CNF54, and CNF96 dimers, it can be observed that the electron coupling integral is negatively correlated with the size of the CNF, i.e., the value of V_{ij} decreases as the size of the CNF increases. This is despite the fact that the interlayer distance is smaller in larger CNF dimers (3.47, 3.42 and 3.39 Å in CNF24 AB, CNF54 AB and CNF96, respectively). The trend corresponds to lower wavefunction amplitudes off-plane in larger flakes. The HOMO orbits are delocalized over the entire flakes, and because they are normalized to one electron charge, the amplitude is lower at a given inter-flake distance, see SI (figure S14). This will lower the overlap integrals, and this effect seems to overweigh the somewhat smaller distances between larger flakes. However, we caution against reading too much into this trend, as it is computed at equilibrium geometry. The charge transfer integral is sensitive to small changes in geometry such as those under thermal vibrations.[176] In SI, we demonstrated that under geometry changes on the order of those expected during thermal motions at $\mathrm{T} = 300K$, the hole transfer rate of CNF54 AB can vary by a factor of two. Therefore, the results above should be considered on the order of magnitude basis. The cyano and -COOH functionalization by and large do not change the hopping rate; the calculation therefore suggests that these functional groups can be used to tune the band alignment in a way not detrimental to charge transport rate. Overall, these results suggest good potential of CNF based molecules as HTM in PSC, but control of their size and functional groups is necessary. In particular, sizes on the order of 1 nm are necessary.

4 Conclusions

In this research, we explored, in a density functional theory computational study, the possibility of carbon nanoflake-based materials as charge transport materials in perovskite solar cells by considering the trends in size, shape, defect, functionalization and packing with respect to their effect on the frontier orbit positions and charge transfer properties of CNF materials, evaluated based on Marcus theory. While other phenomena, not computed here, such as CNF-perovskite interactions, will ultimately affect device performance, we

considered here necessary conditions that must be satisfied by the CNF based material itself and that can serve to narrow down the selection of CNFs.

The results indicate what structural and compositional properties should be achieved to satisfy the conditions for band alignment and charge transport rates. In particular, they suggest that CNFs with hexagonal shapes and diameter around 1.3 nm may obtain the desired band alignment with the $MAPbI_3$ perovskite to act as hole transport materials. Such CNF are also predicted to have good charge transfer rates. In particular, reorganization energies on the order of 0.1 eV and charge transfer rates on the order of 10^{14} s^{-1} are expected to be obtainable. In contrast, the results indicate that band alignment suitable for use as electron transport materials cannot be achieved with any shape or size of CNF (unless heavily functionalized with multiple electron-withdrawing groups). Defects will create gap states or reduce the band gap of the material, therefore should be avoided in synthesis. Most functional groups reduced the band gap as well but have limited effect on the band alignment with perovskite as the LUMO of the CNFs are high enough. The -CN group can bring down both HOMO and LUMO of the CNF, therefore can be used to restore the alignment of CNF's HOMO and perovskite's valance band maximum. Stacking reduces the band gap of CNFs by about half an eV mainly through upshifting the HOMO of the flake, while the resulting band structure remains suitable for selective hole transportation.

5 Author contributions

Ruicheng Li: Calculations, Methodology, Data analysis, Writing - Original draft preparation, Writing - Reviewing and Editing. Keisuke Maeda: Calculations, Data analysis. Keisuke Kameda: Supervision, Writing- Reviewing and Editing. Manabu Ihara: Conceptualization, Resources, Writing- Reviewing and Editing, Project administration, Supervision. Sergei Manzhos: Conceptualization, Methodology, Writing - Original draft preparation, Writing - Reviewing and Editing, Project administration, Supervision.

6 Conflicts of interest

There are no conflicts to declare.

7 Data availability

All the necessary information to reproduce the reported data has been included in the main article. The data supporting this article has been included as part of the ESI.

8 Acknowledgements

This work was supported by JST SPRING (Japan Grant Number JPMJSP2106 and JPMJSP2180) and Science Tokyo Academy of Energy and Informatics (ISE).

9 References

1 M. Jeong, I. W. Choi, E. M. Go, Y. Cho, M. Kim, B. Lee, S. Jeong, Y. Jo, H. W. Choi, J. Lee, J.-H. Bae, S. K. Kwak, D. S. Kim and C. Yang, Stable perovskite solar cells with efficiency exceeding 24.8% and 0.3-V voltage loss, *Science*, 2020, **369**, 1615–1620.

2 N. Li, X. Niu, Q. Chen and H. Zhou, Towards commercialization: the operational stability of perovskite solar cells, *Chem. Soc. Rev.*, 2020, **49**, 8235–8286.

3 J. Y. Kim, J.-W. Lee, H. S. Jung, H. Shin and N.-G. Park, High-Efficiency Perovskite Solar Cells, *Chem. Rev.*, 2020, **120**, 7867–7918.

4 M. A. Green, E. D. Dunlop, M. Yoshita, N. Kopidakis, K. Bothe, G. Siefer and X. Hao, Solar cell efficiency tables (Version 63), *Prog. Photovolt. Res. Appl.*, 2024, **32**, 3–13.

5 W. Peng, K. Mao, F. Cai, H. Meng, Z. Zhu, T. Li, S. Yuan, Z. Xu, X. Feng, J. Xu, M. D. McGehee and J. Xu, Reducing nonradiative recombination in perovskite solar cells with a porous insulator contact, *Science*, 2023, **379**, 683–690.

6 G. Niu, X. Guo and L. Wang, Review of recent progress in chemical stability of perovskite solar cells, *J. Mater. Chem. A*, 2015, **3**, 8970–8980.

7 D. Wang, M. Wright, N. K. Elumalai and A. Uddin, Stability of perovskite solar cells, *Sol. Energy Mater. Sol. Cells*, 2016, **147**, 255–275.

8 I. M. Abdellah, T. H. Chowdhury, J.-J. Lee, A. Islam, M. K. Nazeeruddin, M. Gräetzel and A. El-Shafei, Facile and low-cost synthesis of a novel dopant-free hole transporting material that rivals Spiro-OMeTAD for high efficiency perovskite solar cells, *Sustain. Energy Fuels*, 2021, **5**, 199–211.

9 Y.-C. Chen, S.-K. Huang, S.-S. Li, Y.-Y. Tsai, C.-P. Chen, C.-W. Chen and Y. J. Chang, Facilely Synthesized spiro[fluorene-9,9′-phenanthren-10′-one] in Donor–Acceptor–Donor Hole-Transporting Materials for Perovskite Solar Cells, *ChemSusChem*, 2018, **11**, 3225–3233.

10 Z. Hawash, L. K. Ono, S. R. Raga, M. V. Lee and Y. Qi, Air-Exposure Induced Dopant Redistribution and Energy Level Shifts in Spin-Coated Spiro-MeOTAD Films, *Chem. Mater.*, 2015, **27**, 562–569.

11 H. D. Pham, T. C.-J. Yang, S. M. Jain, G. J. Wilson and P. Sonar, Development of Dopant-Free Organic Hole Transporting Materials for Perovskite Solar Cells, *Adv. Energy Mater.*, 2020, **10**, 1903326.

12 F. Lin, J. Luo, Y. Zhang, J. Zhu, H. Ashraf Malik, Z. Wan and C. Jia, Perovskite solar cells: Li–TFSI and t -BP-based chemical dopant engineering in spiro-OMeTAD, *J. Mater. Chem. A*, 2023, **11**, 2544–2567.
13 S. Wang, M. Sina, P. Parikh, T. Uekert, B. Shahbazian, A. Devaraj and Y. S. Meng, Role of 4-tert-Butylpyridine as a Hole Transport Layer Morphological Controller in Perovskite Solar Cells, *Nano Lett.*, 2016, **16**, 5594–5600.
14 E. J. Juarez-Perez, M. R. Leyden, S. Wang, L. K. Ono, Z. Hawash and Y. Qi, Role of the Dopants on the Morphological and Transport Properties of Spiro-MeOTAD Hole Transport Layer, *Chem. Mater.*, 2016, **28**, 5702–5709.
15 T. Wu, R. Zhuang, R. Zhao, R. Zhao, L. Zhu, G. Liu, R. Wang, K. Zhao and Y. Hua, Understanding the Effects of Fluorine Substitution in Lithium Salt on Photovoltaic Properties and Stability of Perovskite Solar Cells, *ACS Energy Lett.*, 2021, **6**, 2218–2228.
16 S. Li, Y.-L. Cao, W.-H. Li and Z.-S. Bo, A brief review of hole transporting materials commonly used in perovskite solar cells, *Rare Met.*, 2021, **40**, 2712–2729.
17 I. Lee, J. H. Yun, H. J. Son and T.-S. Kim, Accelerated Degradation Due to Weakened Adhesion from Li-TFSI Additives in Perovskite Solar Cells, *ACS Appl. Mater. Interfaces*, 2017, **9**, 7029–7035.
18 H. Zhu, S. Teale, M. N. Lintangpradipto, S. Mahesh, B. Chen, M. D. McGehee, E. H. Sargent and O. M. Bakr, Long-term operating stability in perovskite photovoltaics, *Nat. Rev. Mater.*, 2023, **8**, 569–586.
19 W. Zhou, Z. Wen and P. Gao, Less is More: Dopant-Free Hole Transporting Materials for High-Efficiency Perovskite Solar Cells, *Adv. Energy Mater.*, 2018, **8**, 1702512.
20 J. Luo, C. Jia, Z. Wan, F. Han, B. Zhao and R. Wang, The novel dopant for hole-transporting material opens a new processing route to efficiently reduce hysteresis and improve stability of planar perovskite solar cells, *J. Power Sources*, 2017, **342**, 886–895.
21 M. Li, Z.-K. Wang, Y.-G. Yang, Y. Hu, S.-L. Feng, J.-M. Wang, X.-Y. Gao and L.-S. Liao, Copper Salts Doped Spiro-OMeTAD for High-Performance Perovskite Solar Cells, *Adv. Energy Mater.*, 2016, **6**, 1601156.
22 L. Caliò, J. Follana-Berná, S. Kazim, M. Madsen, H.-G. Rubahn, Á. Sastre-Santos and S. Ahmad, Cu(ii) and Zn(ii) based phthalocyanines as hole selective layers for perovskite solar cells, *Sustain. Energy Fuels*, 2017, **1**, 2071–2077.
23 C. Chen, W. Zhang, J. Cong, M. Cheng, B. Zhang, H. Chen, P. Liu, R. Li, M. Safdari, L. Kloo and L. Sun, Cu(II) Complexes as p-Type Dopants in Efficient Perovskite Solar Cells, *ACS Energy Lett.*, 2017, **2**, 497–503.
24 Y. Bai, Y. Fang, Y. Deng, Q. Wang, J. Zhao, X. Zheng, Y. Zhang and J. Huang, Low Temperature Solution-Processed Sb:SnO2 Nanocrystals for Efficient Planar Perovskite Solar Cells, *ChemSusChem*, 2016, **9**, 2686–2691.
25 J. Zhou, L. Tan, Y. Liu, H. Li, X. Liu, M. Li, S. Wang, Y. Zhang, C. Jiang, R. Hua, W. Tress, S. Meloni and C. Yi, Highly efficient and stable perovskite solar cells via a multifunctional hole transporting material, *Joule*, 2024, **8**, 1691–1706.
26 W. Liu, H. Raza, X. Hu, S. Liu, Z. Liu and W. Chen, Key bottlenecks and distinct contradictions in fast commercialization of perovskite solar cells, *Mater. Futur.*, 2023, **2**, 012103.

27 D. Li, D. Zhang, K.-S. Lim, Y. Hu, Y. Rong, A. Mei, N.-G. Park and H. Han, A Review on Scaling Up Perovskite Solar Cells, *Adv. Funct. Mater.*, 2021, **31**, 2008621.
28 M. Hatamvand, P. Vivo, M. Liu, M. Tayyab, D. Dastan, X. Cai, M. Chen, Y. Zhan, Y. Chen and W. Huang, The role of different dopants of Spiro-OMeTAD hole transport material on the stability of perovskite solar cells: A mini review, *Vacuum*, 2023, **214**, 112076.
29 S. Suragtkhuu, S. Sunderiya, P. Myagmarsereejid, S. Purevdorj, A. S. R. Bati, B. Bold, Y. L. Zhong, S. Davaasambuu and M. Batmunkh, Graphene-Like Monoelemental 2D Materials for Perovskite Solar Cells, *Adv. Energy Mater.*, 2023, **13**, 2204074.
30 H. Xu, F. Yuan, D. Zhou, X. Liao, L. Chen and Y. Chen, Hole transport layers for organic solar cells: recent progress and prospects, *J. Mater. Chem. A*, 2020, **8**, 11478–11492.
31 V. Ferguson, S. R. P. Silva and W. Zhang, Carbon Materials in Perovskite Solar Cells: Prospects and Future Challenges, *ENERGY Environ. Mater.*, 2019, **2**, 107–118.
32 R. He, X. Huang, M. Chee, F. Hao and P. Dong, Carbon-based perovskite solar cells: From single-junction to modules, *Carbon Energy*, 2019, **1**, 109–123.
33 S. Pandey, A. Kumar, M. Karakoti, K. K. Garg, A. Rana, G. Tatrari, B. Singh Bohra, P. Yadav, R. K. Singh and N. Gopal Sahoo, 3D graphene nanosheets from plastic waste for highly efficient HTM free perovskite solar cells, *Nanoscale Adv.*, 2021, **3**, 4726–4738.
34 Z. Ku, Y. Rong, M. Xu, T. Liu and H. Han, Full Printable Processed Mesoscopic CH3NH3PbI3/TiO2 Heterojunction Solar Cells with Carbon Counter Electrode, *Sci. Rep.*, 2013, **3**, 3132.
35 M. Singh, R.-T. Yang, D.-W. Weng, H. Hu, A. Singh, A. Mohapatra, Y.-T. Chen, Y.-J. Lu, T.-F. Guo, G. Li, H.-C. Lin and C. W. Chu, Low-temperature processed bipolar metal oxide charge transporting layers for highly efficient perovskite solar cells, *Sol. Energy Mater. Sol. Cells*, 2021, **221**, 110870.
36 J. Chen, T. Chen, T. Xu, J.-Y. Chang and K. Waki, $MAPbI_3$ Self-Recrystallization Induced Performance Improvement for Oxygen-Containing Functional Groups Decorated Carbon Nanotube-Based Perovskite Solar Cells, *Sol. RRL*, 2019, **3**, 1900302.
37 M. Hadadian, J.-H. Smått and J.-P. Correa-Baena, The role of carbon-based materials in enhancing the stability of perovskite solar cells, *Energy Environ. Sci.*, 2020, **13**, 1377–1407.
38 A. Mei, X. Li, L. Liu, Z. Ku, T. Liu, Y. Rong, M. Xu, M. Hu, J. Chen, Y. Yang, M. Grätzel and H. Han, A hole-conductor–free, fully printable mesoscopic perovskite solar cell with high stability, *Science*, 2014, **345**, 295–298.
39 H. Li, K. Cao, J. Cui, S. Liu, X. Qiao, Y. Shen and M. Wang, 14.7% efficient mesoscopic perovskite solar cells using single walled carbon nanotubes/carbon composite counter electrodes, *Nanoscale*, 2016, **8**, 6379–6385.
40 X. Zheng, H. Chen, Q. Li, Y. Yang, Z. Wei, Y. Bai, Y. Qiu, D. Zhou, K. S. Wong and S. Yang, Boron Doping of Multiwalled Carbon Nanotubes Significantly Enhances Hole Extraction in Carbon-Based Perovskite Solar Cells, *Nano Lett.*, 2017, **17**, 2496–2505.
41 M. Duan, C. Tian, Y. Hu, A. Mei, Y. Rong, Y. Xiong, M. Xu, Y. Sheng, P. Jiang, X. Hou, X. Zhu, F. Qin and H. Han, Boron-Doped Graphite for High Work Function Carbon

Electrode in Printable Hole-Conductor-Free Mesoscopic Perovskite Solar Cells, *ACS Appl. Mater. Interfaces*, 2017, **9**, 31721–31727.
42 Y. Wang, H. Zhao, Y. Mei, H. Liu, S. Wang and X. Li, Carbon Nanotube Bridging Method for Hole Transport Layer-Free Paintable Carbon-Based Perovskite Solar Cells, *ACS Appl. Mater. Interfaces*, 2019, **11**, 916–923.
43 J. Sheng, J. He, D. Ma, Y. Wang, W. Shao, T. Ding, R. Cen, J. He, Z. Deng and W. Wu, Dendritic growth lowers carbon electrode work function for efficient perovskite solar cells, *Carbon*, 2024, **216**, 118577.
44 C. Tian, A. Mei, S. Zhang, H. Tian, S. Liu, F. Qin, Y. Xiong, Y. Rong, Y. Hu, Y. Zhou, S. Xie and H. Han, Oxygen management in carbon electrode for high-performance printable perovskite solar cells, *Nano Energy*, 2018, **53**, 160–167.
45 P. Jiang, Y. Xiong, M. Xu, A. Mei, Y. Sheng, L. Hong, T. W. Jones, G. J. Wilson, S. Xiong, D. Li, Y. Hu, Y. Rong and H. Han, The Influence of the Work Function of Hybrid Carbon Electrodes on Printable Mesoscopic Perovskite Solar Cells, *J. Phys. Chem. C*, 2018, **122**, 16481–16487.
46 L. Fagiolari and F. Bella, Carbon-based materials for stable, cheaper and large-scale processable perovskite solar cells, *Energy Environ. Sci.*, 2019, **12**, 3437–3472.
47 H. Liu, Y. Xie, P. Wei, W. Wang, H. Chen, C. Geng and Y. Qiang, Interface optimization of hole-conductor free perovskite solar cells using porous carbon materials derived from biomass soybean dregs as a cathode, *J. Alloys Compd.*, 2020, **842**, 155851.
48 S. K. Yadav, Hydrophobic compressed carbon/graphite based long-term stable perovskite solar cells, *Mater. Chem. Phys.*, 2021, **268**, 124709.
49 X. Guan, G. Zheng, K. Dai, C. Liu, X. Yan, C. Shen and Z. Guo, Carbon Nanotubes-Adsorbed Electrospun PA66 Nanofiber Bundles with Improved Conductivity and Robust Flexibility, *ACS Appl. Mater. Interfaces*, 2016, **8**, 14150–14159.
50 K. Sun, P. Xie, Z. Wang, T. Su, Q. Shao, J. Ryu, X. Zhang, J. Guo, A. Shankar, J. Li, R. Fan, D. Cao and Z. Guo, Flexible polydimethylsiloxane/multi-walled carbon nanotubes membranous metacomposites with negative permittivity, *Polymer*, 2017, **125**, 50–57.
51 P. Jiang, T. W. Jones, N. W. Duffy, K. F. Anderson, R. Bennett, M. Grigore, P. Marvig, Y. Xiong, T. Liu, Y. Sheng, L. Hong, X. Hou, M. Duan, Y. Hu, Y. Rong, G. J. Wilson and H. Han, Fully printable perovskite solar cells with highly-conductive, low-temperature, perovskite-compatible carbon electrode, *Carbon*, 2018, **129**, 830–836.
52 C. Wang, M. Zhao, J. Li, J. Yu, S. Sun, S. Ge, X. Guo, F. Xie, B. Jiang, E. K. Wujcik, Y. Huang, N. Wang and Z. Guo, Silver nanoparticles/graphene oxide decorated carbon fiber synergistic reinforcement in epoxy-based composites, *Polymer*, 2017, **131**, 263–271.
53 H. Chen and S. Yang, Carbon-Based Perovskite Solar Cells without Hole Transport Materials: The Front Runner to the Market?, *Adv. Mater.*, 2017, **29**, 1603994.
54 D. Bogachuk, S. Zouhair, K. Wojciechowski, B. Yang, V. Babu, L. Wagner, B. Xu, J. Lim, S. Mastroianni, H. Pettersson, A. Hagfeldt and A. Hinsch, Low-temperature carbon-based electrodes in perovskite solar cells, *Energy Environ. Sci.*, 2020, **13**, 3880–3916.
55 Y. Cai, L. Liang and P. Gao, Promise of commercialization: Carbon materials for low-cost perovskite solar cells*, *Chin. Phys. B*, 2018, **27**, 018805.

56 L. Jiang, Y. Peng, T. Xiang, Y. Liu, M. Xu, J. Wang, P.-L. Tremblay and T. Zhang, A counter electrode modified with renewable carbonized biomass for an all-inorganic CsPbBr3 perovskite solar cell, *J. Alloys Compd.*, 2022, **902**, 163725.

57 S. S. Mali, H. Kim, J. V. Patil and C. K. Hong, Bio-inspired Carbon Hole Transporting Layer Derived from Aloe Vera Plant for Cost-Effective Fully Printable Mesoscopic Carbon Perovskite Solar Cells, *ACS Appl. Mater. Interfaces*, 2018, **10**, 31280–31290.

58 N. M. Keppetipola, C. Olivier, T. Toupance and L. Cojocaru, Biomass-derived carbon electrodes for supercapacitors and hybrid solar cells: towards sustainable photo-supercapacitors, *Sustain. Energy Fuels*, 2021, **5**, 4784–4806.

59 A. Abbas, L. T. Mariana and A. N. Phan, Biomass-waste derived graphene quantum dots and their applications, *Carbon*, 2018, **140**, 77–99.

60 H. Liu, C. Geng, P. Wei, H. Chen, S. Zheng, H. Wang and Y. Xie, Improving the performance and stability of large-area carbon-based perovskite solar cells using N, O co-doped biomass porous carbon, *J. Alloys Compd.*, 2022, **912**, 165123.

61 L. Gao, Y. Zhou, F. Meng, Y. Li, A. Liu, Y. Li, C. Zhang, M. Fan, G. Wei and T. Ma, Several economical and eco-friendly bio-carbon electrodes for highly efficient perovskite solar cells, *Carbon*, 2020, **162**, 267–272.

62 B. Thangaraj, P. R. Solomon, S. Chuangchote, N. Wongyao and W. Surareungchai, Biomass-derived Carbon Quantum Dots – A Review. Part 1: Preparation and Characterization, *ChemBioEng Rev.*, 2021, **8**, 265–301.

63 V. G. Matveeva and L. M. Bronstein, From renewable biomass to nanomaterials: Does biomass origin matter?, *Prog. Mater. Sci.*, 2022, **130**, 100999.

64 L. Zhu, D. Shen, C. Wu and S. Gu, State-of-the-Art on the Preparation, Modification, and Application of Biomass-Derived Carbon Quantum Dots, *Ind. Eng. Chem. Res.*, 2020, **59**, 22017–22039.

65 Q. Luo, R. Wu, L. Ma, C. Wang, H. Liu, H. Lin, N. Wang, Y. Chen and Z. Guo, Recent Advances in Carbon Nanotube Utilizations in Perovskite Solar Cells, *Adv. Funct. Mater.*, 2021, **31**, 2004765.

66 Y. Wang, W. Li, T. Zhang, D. Li, M. Kan, X. Wang, X. Liu, T. Wang and Y. Zhao, Highly Efficient (110) Orientated FA-MA Mixed Cation Perovskite Solar Cells via Functionalized Carbon Nanotube and Methylammonium Chloride Additive, *Small Methods*, 2020, **4**, 1900511.

67 V. T. Tiong, N. D. Pham, T. Wang, T. Zhu, X. Zhao, Y. Zhang, Q. Shen, J. Bell, L. Hu, S. Dai and H. Wang, Octadecylamine-Functionalized Single-Walled Carbon Nanotubes for Facilitating the Formation of a Monolithic Perovskite Layer and Stable Solar Cells, *Adv. Funct. Mater.*, 2018, **28**, 1705545.

68 C. Liu, S. Liu, Y. Wang, Y. Chu, K. Yang, X. Wang, C. Gao, Q. Wang, J. Du, S. Li, Y. Hu, Y. Rong, L. Guo, A. Mei and H. Han, Improving the Performance of Perovskite Solar Cells via a Novel Additive of N,1-Fluoroformamidinium Iodide with Electron-withdrawing Fluorine Group, *Adv. Funct. Mater.*, 2021, **2010603**, 1–8.

69 Q.-Q. Chu, Z. Sun, B. Ding, K. Moon, G.-J. Yang and C.-P. Wong, Greatly enhanced power conversion efficiency of hole-transport-layer-free perovskite solar cell via coherent interfaces of perovskite and carbon layers, *Nano Energy*, 2020, **77**, 105110.

70 S. Pitchaiya, N. Eswaramoorthy, M. Natarajan, A. Santhanam, V. Asokan, V. Madurai Ramakrishnan, B. Rangasamy, S. Sundaram, P. Ravirajan and D. Velauthapillai, Perovskite Solar Cells: A Porous Graphitic Carbon based Hole Transporter/Counter Electrode Material Extracted from an Invasive Plant Species Eichhornia Crassipes, *Sci. Rep.*, 2020, **10**, 6835.

71 U. Mukhtar, H. Anwar, Y. Jamil and J. Iqbal, Design and study of novel benzodithiazole-based hole transport materials for improved performance of perovskite solar cells: A DFT approach, *Colloids Surf. Physicochem. Eng. Asp.*, 2024, **702**, 134931.

72 K. Radhakrishna, S. B. Manjunath, D. Devadiga, R. Chetri and A. T. Nagaraja, Review on Carbazole-Based Hole Transporting Materials for Perovskite Solar Cell, *ACS Appl. Energy Mater.*, 2023, **6**, 3635–3664.

73 K. Mahmood, S. Sarwar and M. T. Mehran, Current status of electron transport layers in perovskite solar cells: materials and properties, *RSC Adv.*, 2017, **7**, 17044–17062.

74 W.-J. Chi, Q.-S. Li and Z.-S. Li, Exploring the electrochemical properties of hole transport materials with spiro-cores for efficient perovskite solar cells from first-principles, *Nanoscale*, 2016, **8**, 6146–6154.

75 G. R. Hutchison, M. A. Ratner and T. J. Marks, Hopping Transport in Conductive Heterocyclic Oligomers: Reorganization Energies and Substituent Effects, *J. Am. Chem. Soc.*, 2005, **127**, 2339–2350.

76 B. Xu, E. Sheibani, P. Liu, J. Zhang, H. Tian, N. Vlachopoulos, G. Boschloo, L. Kloo, A. Hagfeldt and L. Sun, Carbazole-Based Hole-Transport Materials for Efficient Solid-State Dye-Sensitized Solar Cells and Perovskite Solar Cells, *Adv. Mater.*, 2014, **26**, 6629–6634.

77 J. Urieta-Mora, I. García-Benito, A. Molina-Ontoria and N. Martín, Hole transporting materials for perovskite solar cells: a chemical approach, *Chem. Soc. Rev.*, 2018, **47**, 8541–8571.

78 S. Gong, H. Li, Z. Chen, C. Shou, M. Huang and S. Yang, CsPbI2Br Perovskite Solar Cells Based on Carbon Black-Containing Counter Electrodes, *ACS Appl. Mater. Interfaces*, 2020, **12**, 34882–34889.

79 P. Avouris, Z. Chen and V. Perebeinos, Carbon-based electronics, *Nat. Nanotechnol.*, 2007, **2**, 605–615.

80 Y. Matsuda, J. Tahir-Kheli and W. A. I. Goddard, Definitive Band Gaps for Single-Wall Carbon Nanotubes, *J. Phys. Chem. Lett.*, 2010, **1**, 2946–2950.

81 X. Zhou, C. Zhao, C. Chen, J. Chen and Y. Li, DFT study on adsorption of formaldehyde on pure, Pd-doped, Si-doped single-walled carbon nanotube, *Appl. Surf. Sci.*, 2020, **525**, 146595.

82 M. P. Anantram and F. Léonard, Physics of carbon nanotube electronic devices, *Rep. Prog. Phys.*, 2006, **69**, 507.

83 H. Tang, T. Xu, X. Qin, K. Zou, S. Lv, J. Fan, T. Huang, L. Chen and W. Huang, Carbon Quantum Dot-Passivated Perovskite/Carbon Electrodes for Stable Solar Cells, *ACS Appl. Nano Mater.*, 2021, **4**, 13339–13351.

84 Y. Zhou, J. Yang, X. Luo, Y. Li, Q. Qiu and T. Xie, Selection, Preparation and Application of Quantum Dots in Perovskite Solar Cells, *Int. J. Mol. Sci.*, 2022, **23**, 9482.

85 A. S. Barnard and I. K. Snook, Modelling the role of size, edge structure and terminations on the electronic properties of graphene nano-flakes, *Model. Simul. Mater. Sci. Eng.*, 2011, **19**, 054001.
86 H. Shi, A. S. Barnard and I. K. Snook, Modelling the role of size, edge structure and terminations on the electronic properties of trigonal graphene nanoflakes, *Nanotechnology*, 2012, **23**, 065707.
87 H. Shi, A. S. Barnard and I. K. Snook, Quantum mechanical properties of graphene nano-flakes and quantum dots, *Nanoscale*, 2012, **4**, 6761–6767.
88 M. Fernandez, H. Shi and A. S. Barnard, Geometrical features can predict electronic properties of graphene nanoflakes, *Carbon*, 2016, **103**, 142–150.
89 M. Fernandez, J. I. Abreu, H. Shi and A. S. Barnard, Machine Learning Prediction of the Energy Gap of Graphene Nanoflakes Using Topological Autocorrelation Vectors, *ACS Comb. Sci.*, 2016, **18**, 661–664.
90 M. Fernandez, A. Bilić and A. S. Barnard, Machine learning and genetic algorithm prediction of energy differences between electronic calculations of graphene nanoflakes, *Nanotechnology*, 2017, **28**, 38LT03.
91 A. Kumar, M. I. Sayyed, D. Punina, E. Naranjo, E. Jácome, M. Khalid Abdulameer, H. Jasim Albazoni and Z. Shariatinia, Graphene quantum dots (GQD) and edge-functionalized GQDs as hole transport materials in perovskite solar cells for producing renewable energy: a DFT and TD-DFT study, *RSC Adv.*, 2023, **13**, 29163–29173.
92 S. Kasi Matta, C. Zhang, A. P. O'Mullane and A. Du, Density Functional Theory Investigation of Carbon Dots as Hole-transport Material in Perovskite Solar Cells, *ChemPhysChem*, 2018, **19**, 3018–3023.
93 Y. Li, W. Zhang, X. Li and Y. Xu, Boosting the photoelectric conversion efficiency of DSSCs through graphene quantum dots: insights from theoretical study, *Mater. Chem. Front.*, 2021, **5**, 5814–5825.
94 V. Sharma and P. K. Jha, Enhancement in power conversion efficiency of edge-functionalized graphene quantum dot through adatoms for solar cell applications, *Sol. Energy Mater. Sol. Cells*, 2019, **200**, 109908.
95 F. López-Urías, J. L. Fajardo-Díaz, A. J. Cortés-López, C. L. Rodríguez-Corvera, L. E. Jiménez-Ramírez and E. Muñoz-Sandoval, Understanding the electrochemistry of armchair graphene nanoribbons containing nitrogen and oxygen functional groups: DFT calculations, *Phys. Chem. Chem. Phys.*, 2020, **22**, 4533–4543.
96 Y. He, L. Yin, R. Zhu and H. Liu, Molecular Design of n-Type Organic Semiconductors with Ultralow Electron Reorganization Energies, *J. Phys. Chem. Lett.*, 2024, **15**, 12083–12089.
97 T. Ando, N. Shimizu, N. Yamamoto, N. N. Matsuzawa, H. Maeshima and H. Kaneko, Design of Molecules with Low Hole and Electron Reorganization Energy Using DFT Calculations and Bayesian Optimization, *J. Phys. Chem. A*, 2022, **126**, 6336–6347.
98 G. Marques, K. Leswing, T. Robertson, D. Giesen, M. D. Halls, A. Goldberg, K. Marshall, J. Staker, T. Morisato, H. Maeshima, H. Arai, M. Sasago, E. Fujii and N. N. Matsuzawa, De Novo Design of Molecules with Low Hole Reorganization Energy Based on a Quarter-Million Molecule DFT Screen, *J. Phys. Chem. A*, 2021, **125**, 7331–7343.

99 J. Staker, K. Marshall, K. Leswing, T. Robertson, M. D. Halls, A. Goldberg, T. Morisato, H. Maeshima, T. Ando, H. Arai, M. Sasago, E. Fujii and N. N. Matsuzawa, De Novo Design of Molecules with Low Hole Reorganization Energy Based on a Quarter-Million Molecule DFT Screen: Part 2, *J. Phys. Chem. A*, 2022, **126**, 5837–5852.

100 A. W. Kuziel, K. Z. Milowska, P.-L. Chau, S. Boncel, K. K. Koziol, N. Yahya and M. C. Payne, The True Amphipathic Nature of Graphene Flakes: A Versatile 2D Stabilizer, *Adv. Mater.*, 2020, **32**, 2000608.

101 D. G. Kvashnin, P. B. Sorokin, J. W. Brüning and L. A. Chernozatonskii, The impact of edges and dopants on the work function of graphene nanostructures: The way to high electronic emission from pure carbon medium, *Appl. Phys. Lett.*, 2013, **102**, 183112.

102 W. Kohn and L. J. Sham, Self-Consistent Equations Including Exchange and Correlation Effects, *Phys. Rev.*, 1965, **140**, A1133–A1138.

103 N. Javed, Z. Cheng, K. Zhu, R. Crichton, H. Maddali, G. Hall, J. Zhang, J. Li and D. M. O'Carroll, Carbon Dot-like Molecular Nanoparticles, Their Photophysical Properties, and Implications for LEDs, *ACS Appl. Nano Mater.*, 2022, **5**, 11741–11751.

104 P. Chakraborty, T. Ma, A. H. Zahiri, L. Cao and Y. Wang, Carbon-Based Materials for Thermoelectrics, *Adv. Condens. Matter Phys.*, 2018, **2018**, 3898479.

105 Q. He, B. Yu, Z. Li and Y. Zhao, Density Functional Theory for Battery Materials, *ENERGY Environ. Mater.*, 2019, **2**, 264–279.

106 L. Tao, Y. Wang, Y. Zou, N. Zhang, Y. Zhang, Y. Wu, Y. Wang, R. Chen and S. Wang, Charge Transfer Modulated Activity of Carbon-Based Electrocatalysts, *Adv. Energy Mater.*, 2020, **10**, 1901227.

107 M. Elstner, D. Porezag, G. Jungnickel, J. Elsner, M. Haugk, Th. Frauenheim, S. Suhai and G. Seifert, Self-consistent-charge density-functional tight-binding method for simulations of complex materials properties, *Phys. Rev. B*, 1998, **58**, 7260–7268.

108 J.-C. Charlier, X. Gonze and J.-P. Michenaud, Graphite Interplanar Bonding: Electronic Delocalization and van der Waals Interaction, *Europhys. Lett.*, 1994, **28**, 403.

109 M. J. Frisch, G. W. Trucks, H. B. Schlegel, G. E. Scuseria, M. A. Robb, J. R. Cheeseman, G. Scalmani, V. Barone, G. A. Petersson, H. Nakatsuji, X. Li, M. Caricato, A. V. Marenich, J. Bloino, B. G. Janesko, R. Gomperts, B. Mennucci, H. P. Hratchian, J. V. Ortiz, A. F. Izmaylov, J. L. Sonnenberg, D. Williams-Young, F. Ding, F. Lipparini, F. Egidi, J. Goings, B. Peng, A. Petrone, T. Henderson, D. Ranasinghe, V. G. Zakrzewski, J. Gao, N. Rega, G. Zheng, W. Liang, M. Hada, M. Ehara, K. Toyota, R. Fukuda, J. Hasegawa, M. Ishida, T. Nakajima, Y. Honda, O. Kitao, H. Nakai, T. Vreven, K. Throssell, J. A. Montgomery Jr., J. E. Peralta, F. Ogliaro, M. J. Bearpark, J. J. Heyd, E. N. Brothers, K. N. Kudin, V. N. Staroverov, T. A. Keith, R. Kobayashi, J. Normand, K. Raghavachari, A. P. Rendell, J. C. Burant, S. S. Iyengar, J. Tomasi, M. Cossi, J. M. Millam, M. Klene, C. Adamo, R. Cammi, J. W. Ochterski, R. L. Martin, K. Morokuma, O. Farkas, J. B. Foresman and D. J. Fox, 2016.

110 R. Dennington, T. A. Keith and J. M. Millam, 2019.

111 P. J. Stephens, F. J. Devlin, C. F. Chabalowski and M. J. Frisch, Ab Initio Calculation of Vibrational Absorption and Circular Dichroism Spectra Using Density Functional Force Fields, *J. Phys. Chem.*, 1994, **98**, 11623–11627.

112 S. Ehrlich, J. Moellmann, W. Reckien, T. Bredow and S. Grimme, System-Dependent Dispersion Coefficients for the DFT-D3 Treatment of Adsorption Processes on Ionic Surfaces, *ChemPhysChem*, 2011, **12**, 3414–3420.

113 B. Hourahine, B. Aradi, V. Blum, F. Bonafé, A. Buccheri, C. Camacho, C. Cevallos, M. Y. Deshaye, T. Dumitrică, A. Dominguez, S. Ehlert, M. Elstner, T. van der Heide, J. Hermann, S. Irle, J. J. Kranz, C. Köhler, T. Kowalczyk, T. Kubař, I. S. Lee, V. Lutsker, R. J. Maurer, S. K. Min, I. Mitchell, C. Negre, T. A. Niehaus, A. M. N. Niklasson, A. J. Page, A. Pecchia, G. Penazzi, M. P. Persson, J. Řezáč, C. G. Sánchez, M. Sternberg, M. Stöhr, F. Stuckenberg, A. Tkatchenko, V. W. -z. Yu and T. Frauenheim, DFTB+, a software package for efficient approximate density functional theory based atomistic simulations, *J. Chem. Phys.*, 2020, **152**, 124101.

114 M. Gaus, A. Goez and M. Elstner, Parametrization and Benchmark of DFTB3 for Organic Molecules, *J. Chem. Theory Comput.*, 2013, **9**, 338–354.

115 M. Gaus, Q. Cui and M. Elstner, DFTB3: Extension of the Self-Consistent-Charge Density-Functional Tight-Binding Method (SCC-DFTB), *J. Chem. Theory Comput.*, 2011, **7**, 931–948.

116 M. Elstner, P. Hobza, T. Frauenheim, S. Suhai and E. Kaxiras, Hydrogen bonding and stacking interactions of nucleic acid base pairs: A density-functional-theory based treatment, *J. Chem. Phys.*, 2001, **114**, 5149–5155.

117 L. Zhechkov, T. Heine, S. Patchkovskii, G. Seifert and H. A. Duarte, An Efficient a Posteriori Treatment for Dispersion Interaction in Density-Functional-Based Tight Binding, *J. Chem. Theory Comput.*, 2005, **1**, 841–847.

118 A. K. Rappe, C. J. Casewit, K. S. Colwell, W. A. Goddard and W. M. Skiff, UFF, a full periodic table force field for molecular mechanics and molecular dynamics simulations, *J. Am. Chem. Soc.*, 1992, **114**, 10024–10035.

119 A. J. Cohen, P. Mori-Sánchez and W. Yang, Insights into Current Limitations of Density Functional Theory, *Science*, 2008, **321**, 792–794.

120 X. Zheng, A. J. Cohen, P. Mori-Sánchez, X. Hu and W. Yang, Improving Band Gap Prediction in Density Functional Theory from Molecules to Solids, *Phys. Rev. Lett.*, 2011, **107**, 026403.

121 R. A. Marcus, On the Theory of Oxidation-Reduction Reactions Involving Electron Transfer. I, *J. Chem. Phys.*, 1956, **24**, 966–978.

122 R. A. Marcus, Electron transfer reactions in chemistry. Theory and experiment, *Rev. Mod. Phys.*, 1993, **65**, 599–610.

123 V. Coropceanu, J. Cornil, D. A. da Silva Filho, Y. Olivier, R. Silbey and J.-L. Brédas, Charge Transport in Organic Semiconductors, *Chem. Rev.*, 2007, **107**, 926–952.

124 Y. Yamada, M. Kawai, H. Yorimitsu, S. Otsuka, M. Takanashi and S. Sato, Carbon Materials with Zigzag and Armchair Edges, *ACS Appl. Mater. Interfaces*, 2018, **10**, 40710–40739.

125 Z.-P. Cao, Y.-J. Zhao, J.-H. Liao and X.-B. Yang, Gap maximum of graphene nanoflakes: a first-principles study combined with the Monte Carlo tree search method, *RSC Adv.*, 2017, **7**, 37881–37886.

126 N. Wohner, P. K. Lam and K. Sattler, Systematic energetics study of graphene nanoflakes: From armchair and zigzag to rough edges with pronounced protrusions and overcrowded bays, *Carbon*, 2015, **82**, 523–537.
127 T. Echigo, M. Kimata and T. Maruoka, Crystal-chemical and carbon-isotopic characteristics of karpatite (C24H12) from the Picacho Peak Area, San Benito County, California: Evidences for the hydrothermal formation, *Am. Mineral.*, 2007, **92**, 1262–1269.
128 A. Camerman and J. Trotter, The crystal and molecular structure of pyrene.
129 W. Zhou, Y. Yin, D. Laniel, A. Aslandukov, E. Bykova, A. Pakhomova, M. Hanfland, T. Poreba, M. Mezouar, L. Dubrovinsky and N. Dubrovinskaia, Polymorphism of pyrene on compression to 35 GPa in a diamond anvil cell, *Commun. Chem.*, 2024, **7**, 1–12.
130 J. Potticary, L. R. Terry, C. Bell, A. N. Papanikolopoulos, P. C. M. Christianen, H. Engelkamp, A. M. Collins, C. Fontanesi, G. Kociok-Köhn, S. Crampin, E. Da Como and S. R. Hall, An unforeseen polymorph of coronene by the application of magnetic fields during crystal growth, *Nat. Commun.*, 2016, **7**, 11555.
131 J. Liu, Y. Yin, B. He, P. Wang, M. Wang, W. Cai, Y. Han, Z. Su, J. Guo, R. Cai, S. Jin, X. Gao, J. Bian and Y. Shi, Focusing on the bottom contact: Carbon quantum dots embedded SnO2 electron transport layer for high-performance and stable perovskite solar cells, *Mater. Today Phys.*, 2023, **33**, 101041.
132 M. Telychko, G. Li, P. Mutombo, D. Soler-Polo, X. Peng, J. Su, S. Song, M. J. Koh, M. Edmonds, P. Jelínek, J. Wu and J. Lu, Ultrahigh-yield on-surface synthesis and assembly of circumcoronene into a chiral electronic Kagome-honeycomb lattice, *Sci. Adv.*, 2021, **7**, eabf0269.
133 M. Ye, G. M. Biesold, M. Zhang, W. Wang, T. Bai and Z. Lin, Multifunctional quantum dot materials for perovskite solar cells: Charge transport, efficiency and stability, *Nano Today*, 2021, **40**, 101286.
134 I. A. Pašti, A. Jovanović, A. S. Dobrota, S. V. Mentus, B. Johansson and N. V. Skorodumova, Atomic adsorption on pristine graphene along the Periodic Table of Elements – From PBE to non-local functionals, *Appl. Surf. Sci.*, 2018, **436**, 433–440.
135 A. M. Valencia and M. J. Caldas, Single vacancy defect in graphene: Insights into its magnetic properties from theoretical modeling, *Phys. Rev. B*, 2017, **96**, 125431.
136 K. M. McCreary, A. G. Swartz, W. Han, J. Fabian and R. K. Kawakami, Magnetic Moment Formation in Graphene Detected by Scattering of Pure Spin Currents, *Phys. Rev. Lett.*, 2012, **109**, 186604.
137 M. Casartelli, S. Casolo, G. F. Tantardini and R. Martinazzo, Spin coupling around a carbon atom vacancy in graphene, *Phys. Rev. B*, 2013, **88**, 195424.
138 A. V. Savin and Y. S. Kivshar, Localized defect modes in graphene, *Phys. Rev. B*, 2013, **88**, 125417.
139 F. Banhart, J. Kotakoski and A. V. Krasheninnikov, Structural Defects in Graphene, *ACS Nano*, 2011, **5**, 26–41.
140 R. Faccio, L. Fernández-Werner, H. Pardo, C. Goyenola, O. N. Ventura and Á. W. Mombrú, Electronic and Structural Distortions in Graphene Induced by Carbon Vacancies and Boron Doping, *J. Phys. Chem. C*, 2010, **114**, 18961–18971.

141 J. Zhu and S. Mu, Defect Engineering in Carbon-Based Electrocatalysts: Insight into Intrinsic Carbon Defects, *Adv. Funct. Mater.*, 2020, **30**, 2001097.
142 X. Yan, Y. Jia and X. Yao, Defects on carbons for electrocatalytic oxygen reduction, *Chem. Soc. Rev.*, 2018, **47**, 7628–7658.
143 Z.-B. Liu, Z.-J. Zhou, Z.-R. Li, Q.-Z. Li, F.-Y. Jia, J.-B. Cheng and C.-C. Sun, What is the role of defects in single-walled carbon nanotubes for nonlinear optical property?, *J. Mater. Chem.*, 2011, **21**, 8905.
144 M. Wang, Q. Wang, T. Liu and G. Wang, Unexpected effect of second-shell defect in iron-nitrogen-carbon catalyst for electrochemical CO2 reduction reaction: A DFT study, *Chin. J. Catal.*, 2024, **66**, 247–256.
145 C. Qiu, L. Jiang, Y. Gao and L. Sheng, Effects of oxygen-containing functional groups on carbon materials in supercapacitors: A review, *Mater. Des.*, 2023, **230**, 111952.
146 Y. Nakao, Metal-mediated C–CN Bond Activation in Organic Synthesis, *Chem. Rev.*, 2021, **121**, 327–344.
147 H. Sun and P. Wu, Tuning the functional groups of carbon quantum dots in thin film nanocomposite membranes for nanofiltration, *J. Membr. Sci.*, 2018, **564**, 394–403.
148 T.-F. Yeh, C.-Y. Teng, S.-J. Chen and H. Teng, Nitrogen-Doped Graphene Oxide Quantum Dots as Photocatalysts for Overall Water-Splitting under Visible Light Illumination, *Adv. Mater.*, 2014, **26**, 3297–3303.
149 H. Liu, Y. Liu and D. Zhu, Chemical doping of graphene, *J Mater Chem*, 2011, **21**, 3335–3345.
150 L. J. A. Koster, S. E. Shaheen and J. C. Hummelen, Pathways to a New Efficiency Regime for Organic Solar Cells, *Adv. Energy Mater.*, 2012, **2**, 1246–1253.
151 Y.-L. Xu, W.-L. Ding and Z.-Z. Sun, How to design more efficient hole-transporting materials for perovskite solar cells? Rational tailoring of the triphenylamine-based electron donor, *Nanoscale*, 2018, **10**, 20329–20338.
152 A. Thomas, R. K. Chitumalla, A. L. Puyad, K. V. Mohan and J. Jang, Computational studies of hole/electron transport in positional isomers of linear oligo-thienoacenes: Evaluation of internal reorganization energies using density functional theory, *Comput. Theor. Chem.*, 2016, **1089**, 59–67.
153 X. Liu, M. Li, R. He and W. Shen, Theoretical investigations on fluorinated and cyano copolymers for improvements of photovoltaic performances, *Phys. Chem. Chem. Phys.*, 2014, **16**, 311–323.
154 J. Lu, J. Yuan, W. Guo, X. Huang, Z. Liu, H. Zhao, H.-Q. Wang and W. Ma, Effects of cyano (CN)-groups on the planarity, film morphology and photovoltaic performance of benzodithiophene-based polymers, *Polym. Chem.*, 2014, **5**, 4772–4780.
155 X. Xu, Y. Gao, Q. Yang, T. Liang, B. Luo, D. Kong, X. Li, L. Zhi and B. Wang, Regulating the activity of intrinsic sites in covalent organic frameworks by introducing electro-withdrawing groups towards highly selective H2O2 electrosynthesis, *Nano Today*, 2023, **49**, 101792.
156 A. Irfan, A. G. Al-Sehemi, M. A. Assiri and S. Ullah, Exploration the effect of metal and electron withdrawing groups on charge transport and optoelectronic nature of schiff base

Ni(II), Cu(II) and Zn(II) complexes at molecular and solid-state bulk scales, *Mater. Sci. Semicond. Process.*, 2020, **107**, 104855.
157 J. M. Lee, J. S. Park, S. H. Lee, H. Kim, S. Yoo and S. O. Kim, Selective Electron- or Hole-Transport Enhancement in Bulk-Heterojunction Organic Solar Cells with N- or B-Doped Carbon Nanotubes, *Adv. Mater.*, 2011, **23**, 629–633.
158 H. S. Jung and N. G. Park, Perovskite solar cells: From materials to devices, *Small*, 2015, **11**, 10–25.
159 G. Giorgi, J.-I. Fujisawa, H. Segawa and K. Yamashita, Cation Role in Structural and Electronic Properties of 3D Organic–Inorganic Halide Perovskites: A DFT Analysis, *J. Phys. Chem. C*, 2014, **118**, 12176–12183.
160 G. Giorgi, J.-I. Fujisawa, H. Segawa and K. Yamashita, Organic–Inorganic Hybrid Lead Iodide Perovskite Featuring Zero Dipole Moment Guanidinium Cations: A Theoretical Analysis, *J. Phys. Chem. C*, 2015, **119**, 4694–4701.
161 R. Chen, B. Luo, C. Liu, X. Ma, L. Qiao, B. Yao, R. Gao, Z. Feng, J. Liu, H. Lin, X. Kong and W. Ren, Polarization Controlled Photocurrent in Perovskite CsGeX3 (X = Cl, Br, I), *J. Phys. Chem. C*, 2023, **127**, 19788–19795.
162 Shahnawaz, S. S. Swayamprabha, M. R. Nagar, R. A. K. Yadav, S. Gull, D. K. Dubey and J.-H. Jou, Hole-transporting materials for organic light-emitting diodes: an overview, *J. Mater. Chem. C*, 2019, **7**, 7144–7158.
163 C. Anrango-Camacho, K. Pavón-Ipiales, B. A. Frontana-Uribe and A. Palma-Cando, Recent Advances in Hole-Transporting Layers for Organic Solar Cells, *Nanomaterials*, 2022, **12**, 443.
164 F. Jin, R. Peng, Y. Qiu, J. Zhang and Z. Ge, Highly Efficient and Stable Organic Solar Cells Enabled by a PEDOT:PSS/HxMoO3 Hybrid Hole Transport Layer, *ACS Appl. Energy Mater.*, 2023, **6**, 9532–9542.
165 S. Khodabakhshi, P. F. Fulvio and E. Andreoli, Carbon black reborn: Structure and chemistry for renewable energy harnessing, *Carbon*, 2020, **162**, 604–649.
166 J.-C. Charlier, X. Gonze and J.-P. Michenaud, First-principles study of the stacking effect on the electronic properties of graphite(s), *Carbon*, 1994, **32**, 289–299.
167 R. D. Heidenreich, W. M. Hess and L. L. Ban, A test object and criteria for high resolution electron microscopy, *J. Appl. Crystallogr.*, 1968, **1**, 1–19.
168 X. Bourrat, Electrically conductive grades of carbon black: Structure and properties, *Carbon*, 1993, **31**, 287–302.
169 X. Chen, H. Sakurai, H. Wang, S. Gao, H.-D. Bi and F.-Q. Bai, Theoretical study on the molecular stacking interactions and charge transport properties of triazasumanene crystals – from explanation to prediction, *Phys. Chem. Chem. Phys.*, 2021, **23**, 4681–4689.
170 J. Yang, S. De, J. E. Campbell, S. Li, M. Ceriotti and G. M. Day, Large-Scale Computational Screening of Molecular Organic Semiconductors Using Crystal Structure Prediction, *Chem. Mater.*, 2018, **30**, 4361–4371.
171 C. Wang, H. Dong, L. Jiang and W. Hu, Organic semiconductor crystals, *Chem. Soc. Rev.*, 2018, **47**, 422–500.

172 Y. Shi, Y. Chang, K. Lu, Z. Chen, J. Zhang, Y. Yan, D. Qiu, Y. Liu, M. A. Adil, W. Ma, X. Hao, L. Zhu and Z. Wei, Small reorganization energy acceptors enable low energy losses in non-fullerene organic solar cells, *Nat. Commun.*, 2022, **13**, 3256.
173 M.-Y. Kuo, H.-Y. Chen and I. Chao, Cyanation: Providing a Three-in-One Advantage for the Design of n-Type Organic Field-Effect Transistors, *Chem. – Eur. J.*, 2007, **13**, 4750–4758.
174 H. Geng, Y. Niu, Q. Peng, Z. Shuai, V. Coropceanu and J.-L. Brédas, Theoretical study of substitution effects on molecular reorganization energy in organic semiconductors, *J. Chem. Phys.*, 2011, **135**, 104703.
175 B. C. Lin, C. P. Cheng and Z. P. M. Lao, Reorganization Energies in the Transports of Holes and Electrons in Organic Amines in Organic Electroluminescence Studied by Density Functional Theory, *J. Phys. Chem. A*, 2003, **107**, 5241–5251.
176 A. Pal, L. K. Wen, C. Y. Jun, I. Jeon, Y. Matsuo and S. Manzhos, Comparative density functional theory–density functional tight binding study of fullerene derivatives: effects due to fullerene size, addends, and crystallinity on band structure, charge transport and optical properties, *Phys Chem Chem Phys*, 2017, **19**, 28330–28343.
177 B. Baumeier, J. Kirkpatrick and D. Andrienko, Density-functional based determination of intermolecular charge transfer properties for large-scale morphologies, *Phys. Chem. Chem. Phys.*, 2010, **12**, 11103.
178 D. Shi, X. Qin, Y. Li, Y. He, C. Zhong, J. Pan, H. Dong, W. Xu, T. Li, W. Hu, J.-L. Brédas and O. M. Bakr, Spiro-OMeTAD single crystals: Remarkably enhanced charge-carrier transport via mesoscale ordering, *Sci. Adv.*, 2016, **2**, e1501491.

Data availability

All the necessary information to reproduce the reported data has been included in the main article. The data supporting this article has been included as part of the ESI.